Synthesis and Investigation on Phase Transition of BaTiO$_3$ and Cr^{3+}-Doped BaTiO$_3$ Nanocrystals

by

Ling Ju

A thesis

presented to the University of Waterloo

in fulfillment of the

thesis requirement for the degree of

Master of Science

in

Chemistry

Waterloo, Ontario, Canada, 2009

I hereby declare that I am the sole author of this thesis. This is a true copy of the thesis, including any required final revisions, as accepted by my examiners.

I understand that my thesis may be made electronically available to the public.

Abstract

Various sizes of $BaTiO_3$ and Cr^{3+}-doped $BaTiO_3$ nanocrystals were synthesized through hydrothermal and solvothermal methods. The applied solvents water, ethanol and benzyl alcohol lead to nanoparticles with average sizes of 200, 10 and 5 nm, respectively. The nanocrystals were treated with trioctylphosphine oxide to remove surface-bound dopant ions, and colloidal free-standing nanocrystals smaller than 10 nm were obtained by using oleic acid as a dispersant surfactant.

The tetragonal-to-cubic phase transition at room temperature of undoped nanocrystalline $BaTiO_3$ has been investigated by powder X-ray diffraction (XRD) and Raman spectroscopy. The size effect of nanoscale $BaTiO_3$ is observed that the tetragonal phase becomes unstable with decreasing particle size. However, we found that ferroelectric tetragonal structure persists to some extent even for particles at 5 nm.

The successful substitution of Ti^{4+} with Cr^{3+} in the host $BaTiO_3$ lattice for all three sizes was achieved at different Cr^{3+}/Ti^{4+} molar ratios. The dopant is found to significantly promote the phase transition, even dominate over the size effect. Ligand-field electronic absorption spectroscopy suggests a subtle change of the octahedral coordinated Cr^{3+} environments between particles at 5 and 10 nm, confirming the structural differences. Preliminary magnetic measurement indicates Cr^{3+} as isolated paramagnetic ions without any chromium clusters or oxides.

The ability to rationally manipulate the ferroelectric properties of $BaTiO_3$ by size and dopants, in combination with possible ferromagnetism induced by incorporating paramagnetic transition metal ions, opens up new opportunities for modern multiferroic materials in information storage technology.

Acknowledgements

Table of Contents

List of Figures

List of Schemes

List of Tables

List of Abbreviations

Cr(acac)$_3$ Chromium (III) Acetylacetonate

DOS   Density of States

EDX   Energy Dispersive X-Ray

FRAM   Ferroelectric Random Access Memory

FWHM   Full Width at Half Maximum

ICP-AES   Inductively Coupled Plasma-Atomic Emission Spectroscopy

LDA   Local Density Approximation

MLCC   Multilayer Ceramic Capacitors

PDF   Pair Distribution Function

PPMS   Physical Properties Measurements System

PTCR   Positive Temperature Coefficient of Resistivity

SAED   Selected Area Electron Diffraction

SEM   Scanning Electron Microscopy

TEM   Transmission Electron Microscopy

TOPO   Trioctylphosphine Oxide

UV/Vis/NIR   Ultra Violet/Visible/Near Infrared

XRD   X-Ray Diffraction

Chapter 1　Introduction

1.1 Properties of Barium Titanate

The family of ferroelectric oxide pervoskites (such as $BaTiO_3$ and $PbTiO_3$) have versatile applications in the electronic industry. Due to its excellent ferroelectric properties, high dielectric constant and relatively simple structure, $BaTiO_3$ has been well studied and widely used in forms of single crystals and ceramics. The application includes multilayer ceramic capacitors (MLCC), ferroelectric random access memory (FRAM), piezoelectric actuators, thermal switches, microwave electronics, *etc.*[1-4] The unique electrical properties of $BaTiO_3$ stem from the elongation of the unit cell along the c-axis, resulting in the ferroelectric tetragonal phase at room temperature.

1.1.1 Crystal Structure of Barium Titanate

Barium titanate has four different phases: paraelectric cubic phase, ferroelectric tetragonal, orthorhombic and rhombohedral phases (Fig. 1.1).

The cubic perovskite phase (space group $Pm\bar{3}m$) is only stable above 120 ^{o}C, with Ba^{2+} ions in the large eightfold coordinated site at (0, 0, 0), Ti^{4+} ions in the octahedrally coordinated site at (1/2, 1/2, 1/2), and O^{2-} ions around each titanium ion at the equipoint (1/2, 1/2, 0). The lattice parameter *a* is 3.996 Å, and the Ti^{4+} ion is as small as 61 pm in radius so that there is room for it to move inside the O_6 cage.[5]

At temperatures between 0 °C and 120 °C, the structure changes to tetragonal phase (space group P4mm) in which the Ti atom moves off-centre along a Ti-O bond, giving a polarization along the [0 0 1] with a value of 26 $\mu C/cm^2$. The original cubic symmetry is distorted with the lengthening of c lattice parameter, and the c/a ratio is 1.011.[5] By choosing the origin at O_{II} position (Fig. 1.1), the displacement data for Ba^{2+}, Ti^{4+} and O_I^{2-} atoms along the c-axis are +0.06 Å, +0.12 Å and -0.03 Å, respectively.[6]

As the temperature falls below 0 °C, an orthorhombic phase (space group C2mm) becomes stable. It is also ferroelectric with the spontaneous polarization parallel to the pseudo-cube edge direction [1 1 0].[6]

At -90 °C, the third phase transition occurs and the lattice symmetry changes to rhombohedral (space group Rm3) with $a = b = c$ and $\alpha = 89.87°$.[7] The ferroelectric polar axis lies along one of the pseudo-cube diagonal directions [1 1 1].
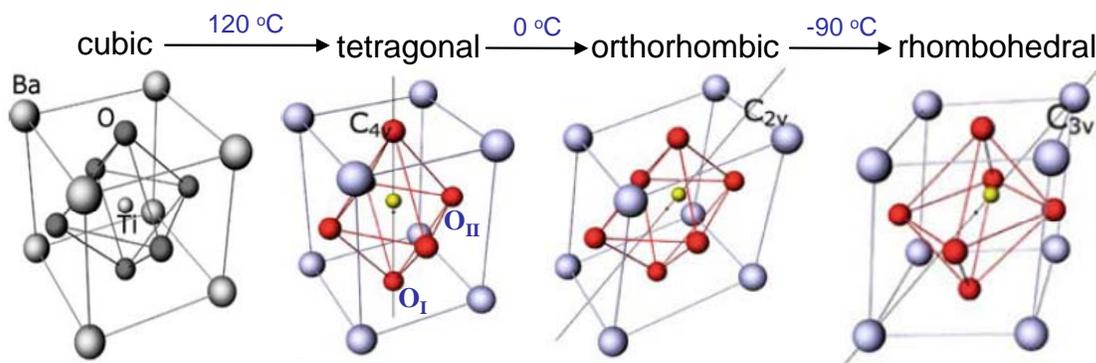
Fig 1.1 Structural transition in $BaTiO_3$[8]

In the three low-temperature ferroelectric phases, the spontaneous polarization results in

remarkable ferroelectric, dielectric, piezoelectric, pyroelectric, electrooptic and nonlinear optical properties.[9] Considering the transition temperature, the cubic-to-tetragonal phase transition is of particular interest. A comparison with related cubic perovskites indicates that the phase transition behavior in $BaTiO_3$ is not universal, but must depend on details of the chemistry and structural thermodynamics of this particular compound.

1.1.2 Origin of Ferroelectricity in Barium Titanate

A lattice of opposite charges is inherently unstable. It is the short-range repulsions between neighboring electron clouds that stabilize ionic materials. In ferroelectric perovskites, besides the short-range repulsions, there is an additional bonding, which might stabilize the distorted phase. In fact, the first-principle calculations in the past twenty years have demonstrated that there exists a delicate balance between the short-range repulsions which prefer the cubic phase, and the long-range electrostatic forces which favor the ferroelectric state.[10]

It is found that in perovskites like $BaTiO_3$ and $PbTiO_3$, the short-range repulsive forces tend to stabilize crystals without off-center displacements. Using the local density approximation (LDA) method to study the electronic structures, Cohen in 1992 found an overlap of the Ti 3d partial densities of states with the O 2p valance bands.[11] This hybridization between the titanium 3d states and the oxygen 2p states is imperative for ferroelectricity, and the hybridization is further enhanced by the ferroelectric distortion. The

interaction between barium and oxygen is largely ionic in nature, and then less affected by the distortion. In addition, according to the characteristic "double-well" potential energy for Ti cation as a function of its position between the oxygen anions (Fig. 1.2), this small cation in ferroelectric perovskite oxides should lower its energy by shifting toward one of the negative O^{2-} ions.[12]
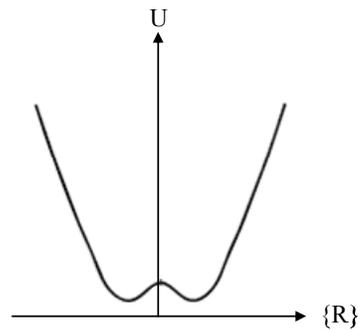
Fig. 1.2 Double-well potential energy as a function of Ti^{4+} position between oxygen anions[12]

Thus the below picture emerged. At low temperature without strain, the lowest energy off-center displacements of Ti^{4+} in $BaTiO_3$ are along the <1 1 1> directions, leading to the rhombohedral ground state. As temperature increases, the off-center displacement disorders over two directions, giving an orthorhombic symmetry. A tetragonal symmetry is formed with disordering over four directions, finally leading to cubic phase at higher temperature.[13]

Another "soft-mode" model also describes the phase transition phenomena in ferroelectric perovskites. Above the Curie temperature T_C, a restoring force tends to pull the Ti cation back to the center if it is displaced. There is a so-called "soft-mode" phonon related to this restoring force, which becomes weaker when the temperature is reduced. Therefore

below the Curie temperature, the phonon frequency is zero and the spontaneous displacement occurs.[12]

This hybridization theory also explains why most ferroelectric oxide perovskites (ABO_3) have B cations with d^0 states, such as Ti^{4+}, Nb^{5+} and Zr^{4+}. It allows for d-hybridization with oxygen, which softens the B-O short-range ion-ion repulsion so that the ferroelectric instability can take place.[7] It appears that in most cases, as soon as the d shell of the B cation is partially occupied, the tendency for it to make a ferroelectric distortion is eliminated.[12] Because of the delicate balance, the phase transition is sensitive to both the defects that modify the short-range interactions, and the carriers that screen the long-range field.[11]

To study the Ti-O hybridization in $BaTiO_3$ better, d-orbital occupation becomes a fundamental parameter in understanding ferroelectricity. Alessio and Nicola[14] used density of states (DOS) calculation to analyze the detailed orbital hybridization and occupation numbers. Because of the Ti 3d and O 2p hybridization, a fraction of Ti d states are occupied and both e_g and t_{2g} states are involved in the hybridization. The occupation numbers of e_g and t_{2g} are 1.16 and 1.15 electrons, respectively. It is suggested that this substantial rearrangement of the charge helps to stabilize the ferroelectric displacements. Further study reveals two kinds of hybridization between O 2p and Ti 3d states: a pd σ hybridization, mixing p_z and d_z^2 orbitals, and a pd π hybridization involving p_x, p_y, d_{xz}, and d_{yz}.[14]

1.1.3 Ferroelectricity of Nanoscale Barium Titanate

In ferroelectric oxides, the spontaneous polarization provides useful applications in memory storage and integrated microelectronics. Recently, the rapid development in MLCC demands the size of $BaTiO_3$ particles to be decreased to tens of nanometers in order to reduce the capacitor dimension.[15] The nanoscaled $BaTiO_3$ devices in ferroelectric nonvolatile memory also promise to increase memory density a thousandfold by reading and writing into single nanoparticles.[16] Thus as the modern electronics industry requires a great decrease in switching time and length scales approaching the manipulation of individual electrons and atoms,[17] nanoscale ferroelectric perovskites with the displacements of individual atoms have proved to be ideal candidates.

In $BaTiO_3$ nanocrystals, the structural and physical properties are strongly dependent on the grain size. Many experiments have indicated that the crystal lattice expands and the phase transition temperature of $BaTiO_3$ decreases as the size of nanoparticles is decreased, with the ferroelectric phase becoming unstable at room temperature when the particle diameter is below a critical size. [9, 15, 18, 19]

However, the investigation on critical size includes a broad range of various theoretical and experimental studies, showing a complex and sometimes controversial picture. Early on, the critical size of $BaTiO_3$ prepared by sol-gel[20] and hydrothermal[21] methods were reported to be around 50 and 90 nm, respectively. Recently, Huang *et al.* observed spontaneous polarization and hysteresis in $BaTiO_3$ nanocrystalline films with grain sizes in the range of

10-30 nm.[2] Spanier *et al.* have even found that some molecular adsorbates can stabilize the ferroelectricity in small-diameter $BaTiO_3$ nanowires, and the critical size of sphere was estimated to be 3 nm.[22] Furthermore, a number of studies have found disorder in $BaTiO_3$ above the transition temperature. Using pair distribution function (PDF), Petkov *et al.* concluded that 5 nm $BaTiO_3$ had a tetragonal-type distortion in the Ti-O distance, even though the average structure was a cubic symmetry.[23] By means of ^{47}Ti and ^{49}Ti NMR, the presence of off-center Ti sites has also been observed in the cubic phase by Zalar and co-workers.[24]

All those differences probably relate to the intrinsic properties of ferroelectric samples with various preparation and size determination methods, considering the transition is very sensitive to lattice defects, strains, surface charges and so on.[18] X-ray diffraction (XRD) results usually support a cubic structure at smaller particle size.[25] Although XRD analysis cannot distinguish between cubic and tetragonal phases, Raman spectroscopy can detect the presence of tetragonal symmetry at small particle sizes. The disagreement suggests that the phase transition behavior in nanoscale $BaTiO_3$ is complex, including both the order-disorder and displacive models.[19]

1.1.4 Possible Causes of Size Effect

Four possible reasons are widely considered to be responsible for the size effect in nanoscale $BaTiO_3$; depolarization effects, the absence of long-range cooperative interactions, structural defects, and elastic constraints.[20]

When a ferroelectric material spontaneously polarizes, charge is compensated to the free surface from both the environment and external circuits, so that the full spontaneous polarization can occur. If a spontaneous polarization is not compensated by charge, however, an internal electric field at the free surface will be formed in the opposite direction of the polarization. Therefore the gradient in polarization from the bulk to the surface provides a source for a depolarization field, which might be strong enough to exceed the free energy reduction for the ferroelectric transition. In the case of single nanocrystals, not enough mechanisms contribute to the compensation, so the depolarization field leads to the thermodynamical instability of ferroelectric phase.[17, 20]

The second view of the cause of size effect in $BaTiO_3$ is related to the driving force stabilizing the ferroelectric distortion. As mentioned previously, the ferroelectric phases results from a delicate balance between the short-range electric repulsions and the long-range electrostatic forces. The Ti 3d and O 2p hybridization is essential to soften the electric repulsions. As the grain size of nanoparticles decreases to a range comparable to the correlation length of the long-range Coulombic interaction, the interactions are too significantly lessened to support the phase transition.[9, 20] Both the lengths parallel and perpendicular to the polarization vector are used to describe the interaction between polar units, and they are stated to be 10-50 nm and 1-2 nm, respectively.[26] That is to say, when crystallite dimensions are reduced to these ranges of sizes, the long-range electrostatic forces are significantly decreased and the ferroelectric phase is expected to transfer to the

paraelectric phase with higher symmetry. In order to create a balance, both the short-range repulsion and Ti-O hybridization are correspondingly reduced.[27] Calculation and simulation in binding energy revealed a character change of Ti-O bonds from covalent to ionic below the critical size,[28] explaining the anomalous lattice expansion with smaller grain size.

Defects are usually considered to be related to the observed cubic structure of $BaTiO_3$ in XRD measurement. It is well known that hydroxyl OH⁻ groups may reside as defects on oxygen sites within $BaTiO_3$ nanoparticles prepared by wet chemical solution methods. The resulting charged defects are very mobile in the matrix and may possess several configurations.[9] Numerous reports demonstrated the existence of internal hydroxyl groups in the hydrothermally prepared $BaTiO_3$ nanoparticles,[29, 30] as well as those synthesized via the sol-gel method.[20, 31] High concentration of charged defects is assumed to result in the disruption of the long-range polar ordering, and the subsequent quenching of the ferroelectricity. It is also demonstrated that the hydroxyl defects can be removed by annealing at high temperature above 800 ^{o}C.[29] However, this will induce changes in the lattice parameters and particle size at the same time.

Lastly, the elastic constraint is believed to cause strong dependences of ferroelectricity on domain structure, especially for the ceramic specimens of grain size with 500-1000 nm.[20] In this range, the energetic cost of a domain structure increases dramatically, and as a result individual grains are unable to develop their full transformation strains, even in the presence of a driving force.[20]

All those proposed factors are reasonable and play important roles in the size effect behavior of nanoscale $BaTiO_3$. They may work together or separately on individual samples. However, deeper investigation and understanding of the mechanism of the phase transition in nanoscale ferroelectric materials are still needed.

1.1.5 Synthetic Methods of Barium Titanate Nanoparticles

0-D $BaTiO_3$ nanocrystalline particles can be synthesized homogeneously with a narrow size distribution. A wide variety of approaches for their syntheses have been reported, with sizes ranging from several nanometers to hundreds of nanometers in diameter depending on the methods and mechanisms.

Traditionally, $BaTiO_3$ nanoparticles are synthesized via high-temperature (above 1000 ^{o}C) calcinations of $BaCO_3$ and TiO_2 powder mixture, which often leads to particles with low purity, as well as uncontrolled and irregular morphologies.[32] Alternatively, high-quality and well-defined $BaTiO_3$ nanocrystals have been developed by wet chemical solution methods, including the coprecipitation method,[33] solution phase decomposition,[34] high-temperature ceramic route,[35] sol-gel processing based on the hydrolysis of metal alkoxide,[20] hydrothermal method, and the fabrication of nanoparticle/polymeric matrix nanocomposites.[36] These preparation strategies have provided easier control of the chemical stoichiometry, better size distribution and relatively low crystallization temperature.

Among them, the hydrothermal method is a low-cost, convenient and most widely

applied approach to $BaTiO_3$ nanoparticles with a one-step process by using an aqueous medium in strongly alkaline solutions. The precursors include a titanium source, such as titanium alkoxide, titanium oxide, or titanium oxide gels, and barium salts such as barium halides, acetate, nitrate, or hydroxide.[32] A typical chemical reaction from inorganic salts can be written as

$$BaCl_2 + TiCl_4 + 4NaOH \rightarrow BaTiO_3 + 4NaCl + 3H_2O$$

giving birth to particles with a diameter around 200 nm.[9] The size and morphology of the particles are highly dependent on the rates of nuclei formation and crystallite growth, which are sensitive to conditions such as concentration, pressure, pH and temperature.[37] Another route is the hydrothermal conversion of titania nanoparticles in barium hydroxide solution, coupling two steps of synthesis of monodispersed titania nanoparticles, and conversion of the prepared titania nanoparticles into spherical nanocrystalline $BaTiO_3$ ranging from 20 to 40 nm.[38]

Recently, the nonaqueous reaction approaches known as "solvothermal" methods have shown advantages in the subtle control of the crystallization and particle growth.[39] Solvents and precursors play essential roles in controlling the particle size, due to the differences in reactivity and capping ability of different groups. Crystalline $BaTiO_3$ particles with diameters smaller than 5 nm have been synthesized by the decomposition of bimetallic alkoxide precursors in organic solvents through the "benzyl alcohol route", where the C-C bond is formed between benzyl alcohol and the precursor ligands.[34] This method was later proved to

be a general synthetic approach for the perovskite family.[40] Xiao Wei and co-workers also

reported the solvothermal synthesis of highly dispersed crystalline $BaTiO_3$ nanoparticles

through the reaction between barium acetate and tetrabutyl titanate in a mixture of

ethylenediamine and ethanolamine, exhibiting better control over particle size.[41]

1.2 Doping Barium Titanate Nanocrystals

1.2.1 Why Dope Barium Titanate Nanocrystals

The intentional introduction of impurities into a host lattice is the process known as

doping,[42] leading to novel phenomena very different from the precursor materials. Bulk

semiconductors are successfully doped to build functional devices, and imparted by new

electrical, optical and magnetic properties.[43, 44] Nanocrystalline semiconductors with unusual

size-dependent optical and electronic behavior,[45] however, are already marketed for

applications as wavelength-tunable lasers, optical gain devices, bioimaging and solar cells.[43, 46] Because their electronic states are confined to a small volume, doping nanocrystals results

in phenomena not found in bulk materials.

Doping $BaTiO_3$ nanoparticles is of great importance in the fabrication of electric and

electronic devices, and a large number of different dopants can be accommodated in the

$BaTiO_3$ lattice. The ionic radius of dopants is the parameter which mainly determines the

substitution site. For ions of the first series of the transition metals, like Cr^{3+}, Mn^{2+}, Mn^{3+},

Fe^{3+}, Co^{3+} and Ni^{2+}, it is well established that they preferentially substitute on the Ti^{4+} site.

The usual mechanism of charge compensation for these ions involves the creation of a stoichiometric amount of oxygen vacancies, so they behave as acceptor dopants.[47] Rare earth ions such as La^{3+} (1.15 Å) and Nd^{3+} (1.08 Å) are incorporated exclusively at the Ba^{2+} (1.42 Å) site, as their size is incompatible with that of Ti^{4+} (0.61 Å). These ions are known to act as donor dopants.[48] For the smaller lanthanide ions from Sm^{3+} to Lu^{3+}, the site occupied by the foreign cation is not exclusive. It is suggested that the ionic radius, dopant concentration, sintering atmosphere and Ba/Ti molar ratio all play crucial roles.[48]

The properties of $BaTiO_3$ can thus be modified through the incorporation with various ions. One of the important applications is the change in the magnitude and character of electrical conductivity induced by appropriate dopants, which leads to semiconducting behavior of $BaTiO_3$ which is an insulator at room temperature. For instance, donor-doping $BaTiO_3$ nanocrystals with trivalent ions (e.g., Y^{3+}, La^{3+}, Nd^{3+}, Sm^{3+}) causes an anomalous increase in electrical resistivity, known as the positive temperature coefficient of resistivity (PTCR) effect.[49] In this regard, electronic compensation is believed to be responsible for the PTCR effect, where reduction of a corresponding number of Ti^{4+} to Ti^{3+} ions occur and the reduced Ti^{3+} ions provide the source of semiconductivity.[50] The effect of a specific dopant on the electrical conductivity of $BaTiO_3$ strongly depends on the substitution site, grain size, doping concentration and defects.[51]

In addition to controlling the electrical properties, the presence of dopants considerably affects the crystal structure of $BaTiO_3$, and therefore the ferroelectric properties. It was widely

reported that small amounts of Mn^{3+} and Fe^{3+} were able to stabilize the hexagonal phase of $BaTiO_3$ after sintering in air, which is a high-temperature phase stable only at temperatures higher than 1460 ^oC.[47, 52-54] The Jahn-Teller distortion is considered as the driving force of the transformation from the cubic to the hexagonal crystal structure. The grain sizes in those cases were in the micrometer range. Buscaglia[48] observed the decrease in room-temperature c/a ratio of Co^{3+}, Fe^{3+} and Ni^{2+}- doped $BaTiO_3$ annealed at 950 and 1350 ^oC, explained as a stabilization of the cubic phase. They attributed this to the creation of oxygen vacancies and also the property of the 3d shell of the transition metal ions. The dopant effect on the crystal structures of $BaTiO_3$ is strongly influenced by the nature of the foreign ions, preparation method, and doping concentration.

Furthermore, a variety of reports describing the magnetic properties of $BaTiO_3$ by impurity doping have been published. In 2001, Nakayama *et al.*[55] performed *ab initio* total energy calculations for transition metal-doped $BaTiO_3$ system and predicted that the Cr^{3+}-, Mn^{2+}-, Mn^{3+}- and Fe^{3+}-doped $BaTiO_3$ are good candidates for ferromagnetic fabrication. Then Co^{3+} implantations in single-crystal $BaTiO_3$ produced magnetic ordering at low temperature, and room-temperature ferromagnetism in Fe^{3+}-doped $BaTiO_3$ single crystalline was observed.[56] Tong recently reported[57] a ferromagnetic behavior at low temperature in the hydrothermally synthesized Mn^{2+}-doped $BaTiO_3$, and ascribed the ferromagnetic mechanism to the exchange coupling interaction between the Mn^{2+} ions and the Ti^{4+} vacancies. These systems thus offer an interesting combination of ferromagnetism induced by transition metal

ions and ferroelectric characteristics of the host $BaTiO_3$ crystals, leading to multiferroicity.

1.2.2 Multiferroism

1.2.2.1. Introduction of Ferroelectricity

The ferroelectric effect was first observed by Valasek in 1921 in the Rochelle salt, which has the formula of $KNaC_4H_4O_6 \cdot 4H_2O$. The effect, however, was not thoroughly studied until a few decades ago when ferroelectric materials came into use in electronic, optical and mechanical devices.

To be ferroelectric, a material must possess a spontaneous dipole moment that can be switched in an applied electric field. A reversal of polarization is considered as a special case of the polarization reorientation.[6] A ferroelectric domain is a homogenous region in which all dipole moments in adjacent unit cells have the same orientation. These domains have random orientations of polarization in the absence of an electric field (Fig. 1.3A), so that there is no overall polarization. When an external electric field is applied, all the domains align in the direction corresponding to it, leading to the full polarization (Fig. 1.3B).

Another important characteristic of ferroelectrics is the ferroelectric hysteresis loop (Fig. 1.4), which arises from the fact that a system does not respond immediately to a given set of external conditions; rather, there is a history dependence.
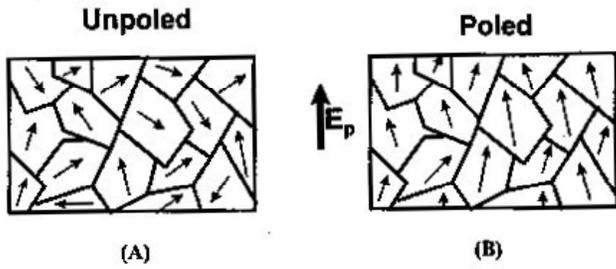
Fig. 1.3 (A) Domains without an external field; (B) ferroelectric domains in a field
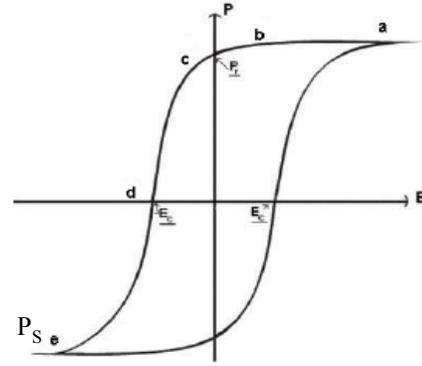
Fig. 1.4 Hysteresis loop for a ferroelectric material

When the electric field is removed at the maximum point of saturation P_s, a remanent polarization P_r remains due to the coupling between the dipoles, which means the material is permanently polarized. When a field is applied in the opposite direction, the polarization will be reversed. A coercive field E_c must be applied to remove the polarization and randomize the dipoles. If the reverse field is increased further, saturation occurs with the opposite polarization.

When the temperature increases, a ferroelectric crystal undergoes a structural phase transition from a ferroelectric phase to a paraelectric phase. The temperature at which the spontaneous polarization disappears is called the Curie temperature, T_C.[6]

1.2.2.2 Introduction of Ferromagnetism

Analogous to ferroelectric materials, a ferromagnetic material undergoes a phase transition from a high-temperature phase that does not have a macroscopic magnetic moment,

to a low-temperature phase which has a spontaneous magnetization even without an applied magnetic field. This critical temperature is called the Curie temperature T_C. As shown in Fig. 1.5, the ferromagnetic material starts in an unmagnetized state due to the presence of domains of magnetization oriented in different directions. As the magnetic field H is increased, the flux density B increases gradually from zero to the maximum value known as saturation induction B_s. When H is reduced to zero after saturation, the induction however only decreases from B_s to B_r, which is called the residual induction. The extra reversed field required to reduce the induction to zero is called the coercivity H_c.[58]
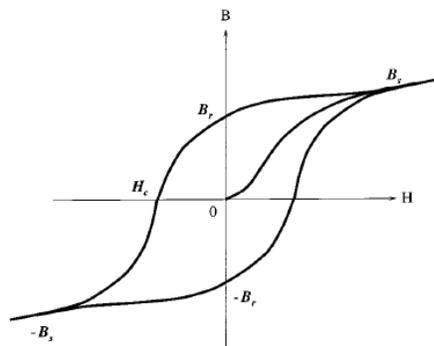
Fig. 1.5 Hysteresis loop for a ferromagnetic material

The saturation magnetization is an intrinsic property of a compound, whereas the remanent magnetization depends on the way a sample has been prepared and treated. Some materials reach their B_s at lower fields than others because the saturation field generally depends on the crystallographic direction, due to spin-orbit coupling. The electron density associated with orbital angular momentum, and therefore chemical bonds, cannot rotate freely with an arbitrary applied field direction. So there exist low fields along certain

crystallographic directions at which B_s is achieved. The direction in which the lowest field is required for saturation is called the easy axis.[59]

The total magnetic moment of a free atom has two contributions from each electron: the angular momentum as the electron orbits the nucleus, and the spin of the electron itself. So in an atom with more than one electron, the total magnetic moment will depend on the spin-orbit, spin-spin and orbit-orbit coupling. When we focus on the moment of an atom, only incomplete electron shells contribute. Once an orbital is more than half full, spins begin to pair up within orbitals and therefore the available magnetic moment decreases. This underlies the existence of magnetic ordering in elements in the middle of the 3d series and the middle of the 4f series.

1.2.2.3 Introduction of Multiferroism

By definition, a single-phased multiferroic material can possess two or all three of the so-called 'ferroic' properties: ferroelectricity, ferromagnetism and ferroelasticity. The current trend, however, is to exclude the requirement for ferroelasticity in practice. So multiferroics now are materials that display both ferroelectric and ferromagnetic behaviors.[60]

Multiferroic materials possess all the potential applications of both their parent ferroelectric and ferromagnetic materials. In addition, a whole range of new applications can be envisaged. The ability to utilize either the electric or magnetic polarization allows an additional degree of freedom in device design, and, for example, provides the unique

opportunity to encode information independently in electric polarization and magnetization, obtaining four possible different logic states (Fig. 1.6).[12]
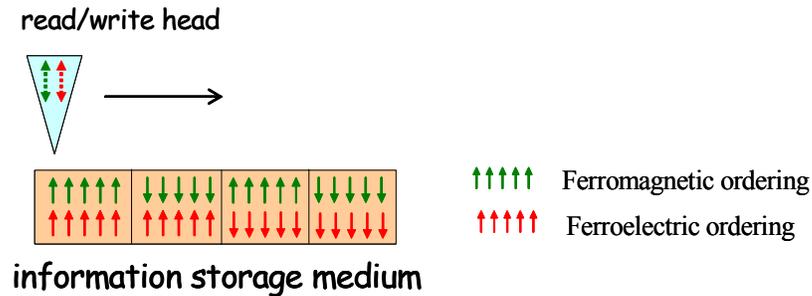
Fig. 1.6 Schematic of the storage states in multiferroics

Also, recent research on multiferroics has shown that ferroelectricity and magnetism not only coexist in the same material, but also couple with each other so that the magnetic degree of freedom can be manipulated by an electric field and the electric degree of freedom can be manipulated by a magnetic field, known as magnetoelectric effect.[61] This in principle permits data to be written electrically and read magnetically. Considering FRAM is hard to read and magnetic data storage needs large local magnetic fields to write, the coupling technology would exploit the best aspects of both ferroelectric and ferromagnetic data storage. Significant materials are still under research and a lack of experimental data still remains.

1.2.3 Doping Mechanisms

Despite doping successes, the low concentration of incorporated dopants remains a

problem in many studies of nanocrystals doping. The inserted impurities seemed to be excluded from the internal volumes of the host nanocrystals. The answer to such problems often lies in between kinetics and thermodynamics.

One proposed doping mechanism is known as "self-purification" (Fig. 1.7A), suggesting that the impurity solubility is much lower in nanocrystals than in the bulk. By assuming the system is under thermodynamic equilibrium, Dalpian and Chelikowsky[62] calculated the relative defect formation energy in the Mn-doped CdSe sample, elucidating the stability and population of the dopants under equilibrium. The formation energy increases as the size of nanocrystals decreases, showing that more energy is required to insert impurities into small nanocrystals than the larger ones, and impurities will be easily expelled from the clusters. This assumption based on thermodynamic equilibrium, however, is strongly dependent on the diffusion of impurity atoms, which works well for solid or gas-phase syntheses at high temperature where most dopants diffuse rapidly.

In colloidal growth typically around 300 ^{o}C, diffusion of some impurities in semiconductor is sometimes very low.[42] This suggests that thermal equilibrium is not established, and kinetic factors will instead control the doping. Erwin *et al.* showed a "trapped dopant" mechanism,[43] in which the initial adsorption of impurities on the nanocrystal surface during growth controls the doping.[42] After adsorbing on the surface of the nanocrystal, the impurity was covered by additional materials. So the doping efficiency is determined by surface morphology, nanocrystal shape, and surfactants in the growth solution.

A. Self-Purification
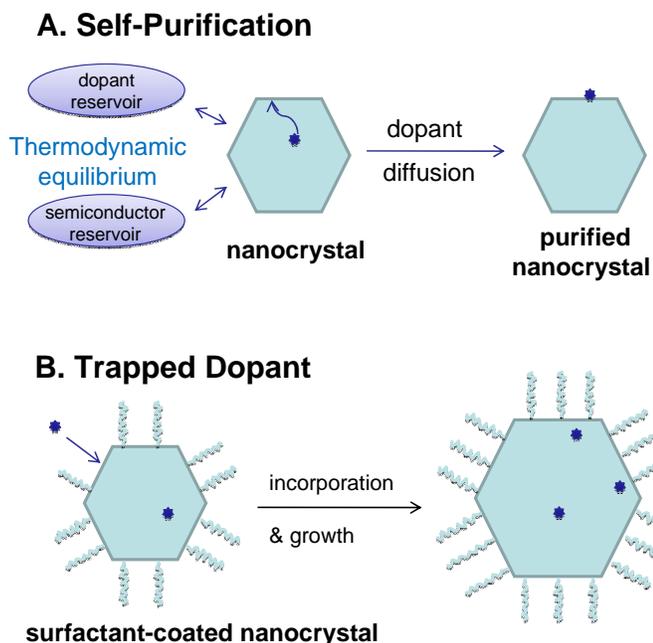
B. Trapped Dopant

Fig. 1.7 Two models used to explain doping in nanocrystals[43]

Bryan *et al.* summarized detailed mechanisms of this "trapped dopant" crystal nucleation and growth.[46] In a wet chemical synthesis of colloids, the classical LaMer model[63] is used to describe undoped crystal nucleation and growth (Fig. 1.8A), where a continuous influx of precursors is assumed. When the concentration of precursors in solution reaches a critical level of supersaturation (C_{ss}), spontaneous phase segregation occurs. Then the dissolved precursor concentration in solution is consumed until it is below the level required for nucleation, but remains above the saturation concentration (C_s) such that the crystals continue to grow. The exothermicity of lattice formation provides the driving force for spontaneous phase transition. This force, ΔF_V, is described by the free energy difference between solvated and crystalline forms of the materials. When the particles are very small, the surface free

energy γ needs to be considered, which destabilizes the crystal toward solvation in proportion to the crystal's surface area.[64] Thus the change of Gibbs free energy for the reaction is described as

$$\Delta G = 4\pi R^2 \gamma + 4/3\pi R^3 \Delta Fv$$

The solid line in Fig. 1.8B shows the plot of ΔG versus crystal radius. The barrier of ΔG^* defines the critical radius R^*, and dR/dt represents the growth rate. When $R < R^*$, the particles redissolve in the solution ($dR/dt < 0$) and when $R > R^*$, they will survive to grow into larger crystals. Though simple regardless of quantum chemical and dynamics consideration, this classical nucleation model describes the basic principal of this chemistry in a valuable way.
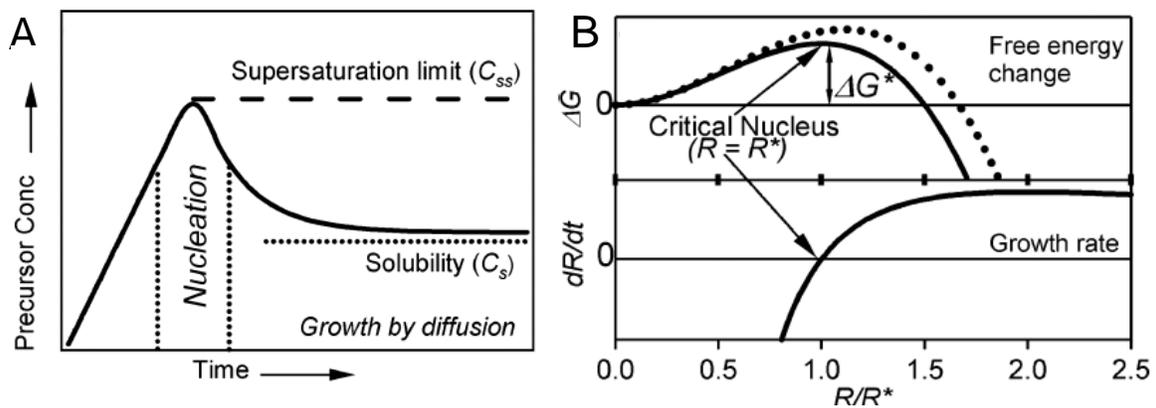
Fig. 1.8 (A) LaMer Model for nucleation and growth of crystallites; (B) Classical nucleation model (solid line) and nucleation in the presence of dopants (dashed line) showing Gibbs free energy change (ΔG) and growth rate[46]

In the scenario of doping, the general principle of the classical model remains unchanged. However, as the introduction of dopants, the extra strain of the lattice contributes as a sacrifice of the driving force for lattice formation.[46] As shown in Fig. 1.8B (dashed line), the reduction of ΔF_V leads to the increase of activation barrier ΔG^* and thus the dimension of the critical radius. In this sense, it is more difficult for the doped crystal to nucleate than it was for the pure host crystal itself. In fact, the greater the dopant-host incompatibility is, the harder the critical nucleus containing impurities will form. This explains the observation that a majority of the critical nucleus is made of pure host materials.

Besides the influence of dopants on nanocrystal nucleation, Bryan *et al.* also discussed the effect of impurities on the nanocrystal growth.[46] They concluded that dopant incorporation is kinetically uncompetitive with nanocrystal growth at early stages of growth, when lattice nutrient is abundant and growth occurs rapidly. Further inspection shows a very slow solvation of surface-bond dopants, indicating the necessity of the dopants' irreversible binding to the nanocrystal surface. In this case, however, this surface binding was found to pin step edges, inhibiting further crystal growth, hence reducing the nanocrystal diameters.[65, 66] By raising the effective specific interfacial energy, the impurity ion near the surface of a crystal can shift the equilibrium towards solvation. This is understood as the reason for the truncation of nanocrystal growth by impurities.[46] In general, the chemistry of the dopants is indeed essential, as well as other factors such as types of ligands in the reactions.

1. 3 Statement of Goals

I have synthesized nanosized $BaTiO_3$ in different sizes as an attempt to understand the finite size effect on the ferroelectricity in nanoscale materials. In this case, highly dispersed nanocrystals enable precise investigation into the structure of individual nanoparticles, and thus the dependence of ferroelectricity on the particle size.

I have chosen Cr^{3+}-doped $BaTiO_3$ as a candidate to investigate the dopant effect on the structure and properties of ferroelectric host lattices. Considering Mn^{2+}, Mn^{3+} and Fe^{3+} have been successfully doped into $BaTiO_3$ single crystals, Cr^{3+} is of interest with a simple d^3 system, which has induced robust ferromagnetism in other oxides.[67, 68] Also, Cr^{3+} is kinetically inert with a high affinity of six-coordinate sites if substituted for Ti^{4+} ions in $BaTiO_3$.

Chapter 2   Experimental Section

2.1 Materials

Barium rods (Ba, 99%), titanium (IV) isopropoxide (Ti{OCH(CH$_3$)$_2$}$_4$, 98%), chromium (III) acetylacetonate (Cr(C$_5$H$_7$O$_2$)$_3$, Cr(acac)$_3$, 97.5%), chromium (III) chloride hexahydrate (CrCl$_3$·6H$_2$O) and barium titanate as a bulk standard (BaTiO$_3$, 99%) were purchased from Strem Chemicals. Trioctylphosphine oxide (TOPO, 90%) and benzyl alcohol (C$_6$H$_5$CH$_2$OH 99%) were obtained from Aldrich. Oleic acid (CH$_3$(CH$_2$)$_7$CH=CH(CH$_2$)$_7$COOH) and toluene (99.98%) was purchased from EMD Chemicals. For the solvothermal treatment, Parr acid-digestion bombs with 45 mL Teflon liners were used.

2.2 Synthesis

2.2.1 Synthesis BaTiO$_3$ nanoparticles with different sizes

In order to adjust the size of BaTiO$_3$ from several to several hundreds of nanometers, we applied three different solvents to the hydrothermal synthesis procedures. They are benzyl alcohol, ethanol and water.

BaTiO$_3$ nanocrystals around 4 nm are synthesized by a modified literature procedure[33] carried out in an inert atmosphere. In a typical synthesis, 3 mmol of metallic barium is dissolved in 20 mL anhydrous benzyl alcohol at 80 $^{\circ}$C until a slightly yellowish solution is obtained. The solution was cooled to room temperature, followed by adding 1 mol equivalent

of titanium (IV) isopropoxide. The mixture is then stirred overnight. After a gelled precipitate formed, the precursor mixture was transferred to a Parr bomb under an inert atmosphere, and heated at 200 $^{\circ}$C for 48 h.

As far as the synthesis of larger BaTiO$_3$ nanocrystals is concerned, a slightly different condition has been adopted. The gelled suspension in the 'benzyl alcohol route' mentioned above is centrifuged, and the supernatant is substituted with degassed ethanol or deionized water. After mixing the precipitate with the new solvent, the total volume is adjusted to be 20 mL. Finally, this suspension is sealed in the bomb and heated at the same condition as in the 4 nm nanoparticles synthesis. The sizes of the resultant products for the solvents of ethanol and water are about 10 nm and 100 nm, respectively.

2.2.2 Synthesis of Cr^{3+}-Doped BaTiO$_3$ nanoparticles

Cr^{3+}-doped BaTiO$_3$ nanoparticles are prepared using the same methods described for the synthesis of pure BaTiO$_3$ nanoparticles with solvents benzyl alcohol and ethanol, but in the presence of various amounts of Cr(acac)$_3$ in the precursor mixture. The starting molar ratio of Cr(acac)$_3$ to Ti isoproxide in the precursor was varied from 0.05 to 0.2.

Due to the low solubility of Cr(acac)$_3$ in water, besides the addition of Cr(acac)$_3$ together with metallic Ba (**method A**), another methodology was performed. Different amounts of CrCl$_3$·6H$_2$O were dissolved in water and used to replace the benzyl alcohol supernatant in the synthesis of undoped BaTiO$_3$ using 'water-synthesis route', named as **method B**.

2.2.3 Surfactant Treatment

When the reaction was finished, the bomb was cooled to room temperature. The resulting nanoparticles were collected by centrifugation and washed three times with ethanol. To clean the surface and remove any surface-bound dopant ions, both the pure and doped as-synthesized samples were suspended in melted trioctylphospine oxide (TOPO) and heated at 150 ^{o}C for 1 h.[69] Precipitation with ethanol three times followed. This TOPO cleaning and precipitation procedure was repeated three times, yielding TOPO-capped Cr^{3+}-doped $BaTiO_3$ nanoparticles. After drying under ambient condition, the powder suitable for XRD and Raman measurements was obtained.

To get the colloidally stable suspension of pure and doped $BaTiO_3$ nanoparticles, oleic acid ($CH_3(CH_2)_7CH=CH(CH_2)_7COOH$) was selected as the dispersive surfactant among many dispersants.[3, 4] The TOPO-capped nanocrystals were heated in oleic acid at 100 ^{o}C for half an hour, followed by wash and re-precipitation with ethanol. This step allowed for capping of the nanoparticles with oleic acid. The obtained nanocrystals were then suspended in hexane or toluene. A clear solution was obtained for further application.

2.3 Characterization and Measurements

2.3.1 X-ray Diffraction

Powder X-ray diffraction (XRD) patterns were recorded in an INEL diffractometer with a position-sensitive detector, utilizing monochromatized $Cu-K_\alpha$ radiation.

As the crystallite size decreases, the width of the diffraction peak increases. This is because not enough crystal planes exist to produce complete destructive interference in small crystallites, therefore broadened peaks can be seen.[70] The Debye-Scherrer formula enables the thickness of a crystallite to be calculated from the peak widths and positions:

$$T = \frac{C\lambda}{B\cos\theta}$$

where T is the crystallite thickness, λ is the wavelength of the X-rays (1.5418 Å), θ is the diffraction angle in radians, and B is the full-width at half-maximum (FWHM). However, this is at best an approximation of average particle size only applied to particles smaller than 40 nm.

2.3.2 Raman Spectroscopy

Raman spectroscopy was performed at room temperature with a Renishaw 1000 spectrometer using He-Ne laser with the excitation wavelength of 632.8 nm. The radiation source employed was 10% of the total output power (40 mW). Prior to the measurement, the spectrometer was calibrated using a silicon foil.

When a photon collides with a molecule, three types of scattering can be observed as shown in Fig. 2.1. In Rayleigh scattering, also referred to as elastic scattering, a photon interacts with a molecule, polarizing the electron cloud and exciting electrons to a 'virtual' energy state. This is extremely short lived and the molecule soon relaxes to its ground state, releasing a photon with the same frequency as the initial one.

Raman scattering is different in that it is inelastic, which is based on the Raman effect that the frequency of the reemitted photons is shifted up or down in comparison with the original monochromatic frequency.

If the molecule drops form the virtual state back to a higher energy vibrational state, then the scattered photon has less energy than the incident photon and therefore a longer wavelength. This is called Stokes scattering. In contrast, if the molecule begins with a vibrational state and drops back to its ground state after scattering, the scattered photon has more energy and shorter wavelength. This is called anti-Stokes scattering.
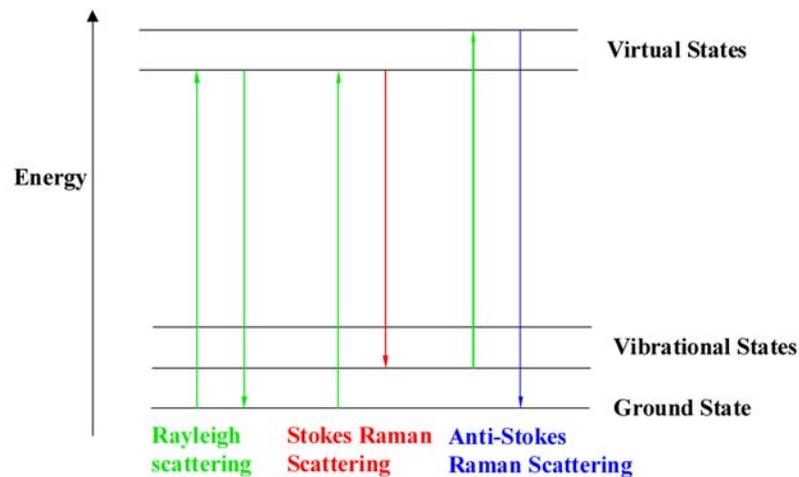
Fig. 2.1 Three different forms of scattering

The shift due to the Raman effect is determined by the spacing between the vibrational states and the ground states. Only about 0.001% of the incident light produces inelastic Raman signal, so this is usually swamped by the far more prominent Rayleigh scattering.

Normally in Raman spectroscopy, only the Stokes scattering of the spectrum is used, due to its greater intensity. The Raman spectrum is more sensitive to the lengths, strengths, and arrangement of chemical bonds in a material, rather than to the chemical composition.[71]

2.3.3 Electron Microscopy

The morphology of larger particles synthesized by the 'water route' was studied by scanning electron microscopy (SEM) using a LEO FESEM 1530 microscope operating at 5 kV.

Transmission electron microscopy (TEM) was performed with a JEOL-2010F microscope operating at 200 kV. Gatan Digital Micrograph software was used to measure d-spacings from TEM images.

2.3.4 UV-Vis Absorption Spectroscopy

The Optical absorption spectra were collected with Varian Cary 5000 ultraviolet/visible/near-infrared (UV/vis/NIR) spectrophotometer using 1 cm path-length quartz cuvettes.

We are particularly interested in ligand-field electronic absorption spectroscopy of transition-metal dopants. This technique allows us to quantitatively describe the speciation of transition metal ions including their oxidation states and geometries. The five d-orbitals of transition metals have the same energy when the atom is isolated. However, the energy will

change when ligands are coordinated. Consider an octahedral geometry in which six ligands surround a metal ion. In a complex, the two d-orbitals d_{x2-y2} and d_{z2} that point along the x, y, z axes are raised in energy, while the other three d_{xy}, d_{zx}, d_{yz} orbitals which point between the ligands are less repelled and lowered in energy (Fig. 2.2A). The splitting between these d-orbitals (Δ_o) has the energy corresponding to the absorption of visible part of the spectrum. Therefore, most transition metal complexes are colored. Transitions of Δ_o from the lower to higher d orbitals are called d-d transitions, of ligand-field transitions.

A Tanabe-Sugano diagram is a graph which plots the energy of different spectroscopic terms (on the y-axis) against the size of the ligand field (on the x-axis), which can be used to predict the energy of any absorption bands in the UV-visible spectra of transition metal complexes. Fig. 2.2B shows an example of d-d transitions in d^3 metal (such as Cr^{3+} ion) complexes. The labeled transition corresponds to a promotion of one of the t_{2g} electrons to the e_g orbitals.
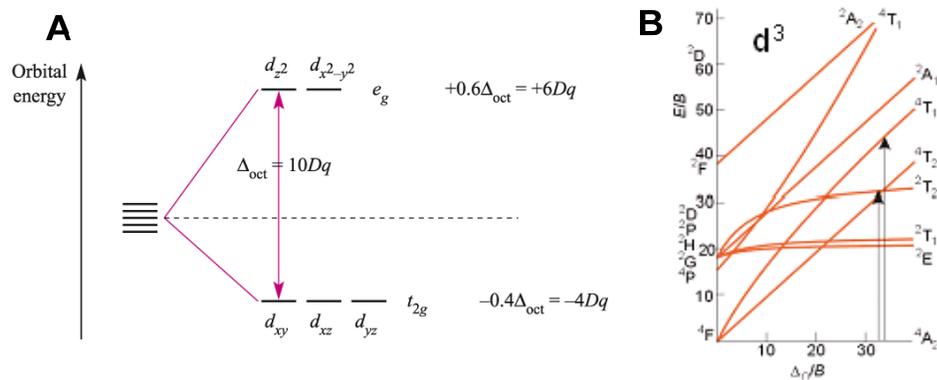
Fig. 2.2 (A) Octahedral ligand field; (B) Tanabe-Sugano diagram for d^3 configuration

In this project, the doped transition metals can be detected by this technique, to investigate how they incorporate into the host nanocrystalline lattices. By assigning the peaks to certain transitions, we can determine the doping speciation, both in the aspects of geometries and oxidation states of the dopant ions. If dopant metals ended up on the surfaces of the nanocrystals, resulting in discrepancies in the binding environment, it is also detectable from the spectra.

2.3.5 Magnetic Measurements

The magnetization was measured with the physical property measurement system (PPMS, Quantum Design) in ACMS mode, with a helium cooling system, allowing a wide range of temperatures from 2 to 400 K and magnetic fields up to $\pm$ 9 Tesla. The overall effective magnetic moment can be measured as a function of temperature, or the applied magnetic field from a positive to a negative one, monitoring magnetic properties.

Chapter 3 Study of Undoped BaTiO$_3$ Nanocrystals

3.1 Structures Determined by X-ray Diffraction

Typical XRD patterns of BaTiO$_3$ nanoparticles synthesized in water, ethanol and benzyl alcohol are given in Fig. 3.1. Commercial bulk BaTiO$_3$ powder was also studied for comparison. All the as-synthesized samples are consistent with BaTiO$_3$ structures. Only a minor contribution of BaCO$_3$ byproduct was detected in the ethanol synthesized sample (marked with asterisks), which is a very common impurity in the synthesis of BaTiO$_3$ and can be removed through an acid washing process.[72]
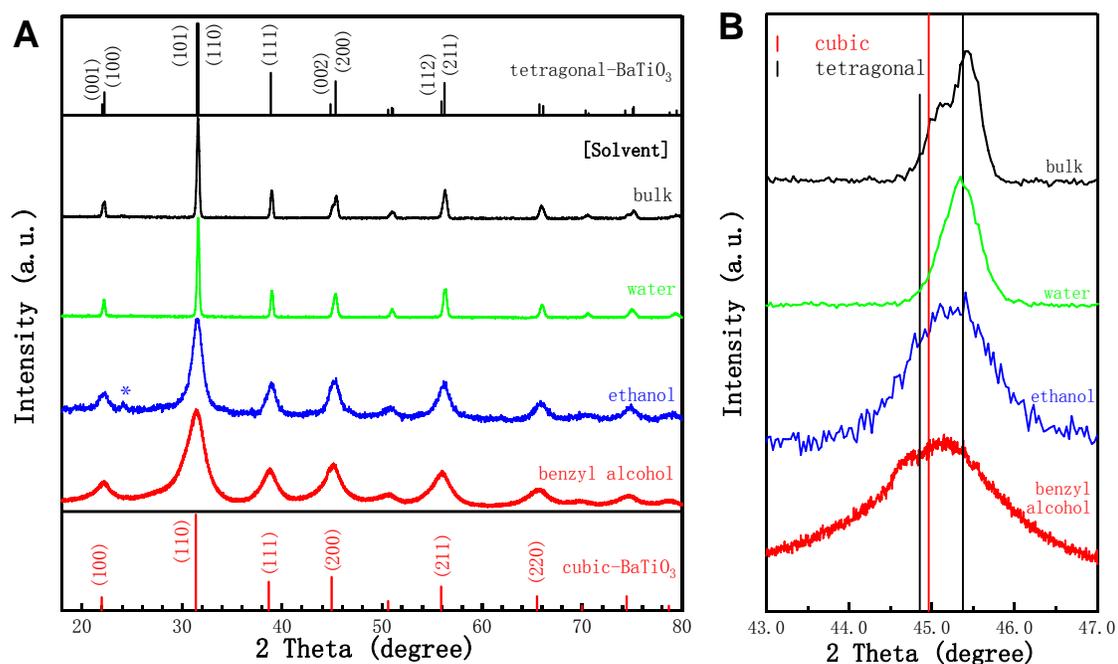
Fig. 3.1 (A) XRD patterns of BaTiO$_3$ particles prepared in different solvents and commercial bulk BaTiO$_3$ powder for comparison. The vertical lines represent the standard patterns of bulk cubic-BaTiO$_3$ (bottom, JCPDS No. 31-0174) and tetragonal-BaTiO$_3$ (top, JCPDS No.

05-0626). * corresponds to orthorhombic $BaCO_3$; (B) Enlarged XRD patterns between 43.0^o and 47.0^o.

Apparently, the sizes of the $BaTiO_3$ nanocrystals derived from different solvents differ significantly. The peaks become broader and the full width at half of maximum intensity increases while samples are prepared in different solvents from water, ethanol to benzyl alcohol, indicating a gradual decrease in the crystallite sizes. From the Debye-Scherrer equation, we can account the broadening of the (100), (110) and (111) diffraction lines to calculate that the average particle sizes are 4.0 nm and 7.5 nm for the ethanol- and benzyl alcohol- synthesized nanocrystals, respectively. The instrumental line width, however, limits the determination of water synthesized particle size.

Since the cubic and tetragonal structures of $BaTiO_3$ are closely related, their powder XRD patterns are extremely similar, making it difficult to distinguish between them. The commonly used characteristic peak in the diffraction pattern ranges between $2\theta = 40^o - 50^o$ region, where the single cubic (200) line splits into two tetragonal peaks (200) and (002). However, it is still difficult to assign the crystal symmetry using conventional X-ray diffractometers in our case due to the line broadening caused by the size effect. Despite these difficulties, closer inspection of the partial enlargement patterns still reveals some interesting findings. As shown in Fig. 1B, bulk $BaTiO_3$ exhibits apparent splitting of the (200) peak and therefore strong tetragonality, considering $BaTiO_3$ is in a tetragonal phase at room

temperature. The small shoulder around 45° does not match exactly with the standard tetragonal (002) line, probably due to the slightly different c/a ratios in different bulk samples.

Compared with peaks of bulk $BaTiO_3$ which possesses the highest amount of tetragonality, two factors are used to analyze the structure of the as-synthesized nanocrystals; peak shift and splitting. Generally speaking, the splitting is not distinct in all the nanoparticles, indicating a possible increase in the degree of cubic phase as the grain size decreases of nano-scale. Also, from particles synthesized in water to those in ethanol and benzyl alcohol, the peak position center of gravity shifts from tetragonal (200) line (black) to cubic (200) line (red), revealing a lattice expansion and a structural change from tetragonal to cubic when the particle size is decreased.

However, considering the tetragonal distortion $(c-a)/a$ of only 1% even in bulk $BaTiO_3$ materials, XRD is limited in the resolution of peak splitting owing to extensive broadening of Bragg reflections, in particular for nanocrystalline materials.[73] In this case, the detailed peak shape may be an indication of the structures. Notice the slightly asymmetric shape of peaks in all three nanoscale samples. This indicates a possible splitting clue to some extent, caused by the tetragonality itself, or attributed to the effect of coexistence of both tetragonal and cubic phases, which is difficult to quantify because of the peak broadening and the mixture of two phases.

Furthermore, a relatively distinct asymmetric shape is found in the (200) peak of benzyl alcohol synthesized nanoparticles, indicating the presence of some tetragonality even in

particles as 4 nm. Ahn[17], Petkov[23] and Huang[2] also reported the tetragonality of $BaTiO_3$ at similar sizes. In fact, Smith *et al.* found[18] that though more similar to cubic phase in lattice parameters and *c/a* ratio, smaller $BaTiO_3$ nanoparticles surprisingly have more titanium displacements inside of the lattice, and they attributed it to the increased cell volume in cubic phase which provides more space for titanium off-centering, and the reduction in periodicity in the lattice which diminishes the restoring Coulombic force on movable atoms. In terms of the nanoparticles synthesized in benzyl alcohol, the shift to cubic line demonstrates the tetragonal-to-cubic structure revolution regarding the *c/a* ratio, and the asymmetric shape of the (200) peak may be a result of the Ti displacement in small particles. However, more study is needed to clarify and refine the crystal structures.

3.2 Morphology

SEM and TEM were used to investigate the morphology of the obtained $BaTiO_3$ nanocrystals. Presented in Fig. 3.2, 3.3 and 3.4 are typical SEM and TEM images of $BaTiO_3$ nanoparticles synthesized in water, ethanol and benzyl alcohol, respectively. Morphologies of all the three sized particles appear to be consistent without larger particles. The water-synthesized particles have a relatively larger grain size as we expected, which is in the range from 100 to 250 nm, and the mean particle size is determined to be around 200 nm. Meanwhile, particle diameters of the ethanol- (Fig. 3.3) and benzyl alcohol- (Fig. 3.4) synthesized samples lie within the range of 7.5-10 and 4-5 nm, which are in good agreement

with XRD results.
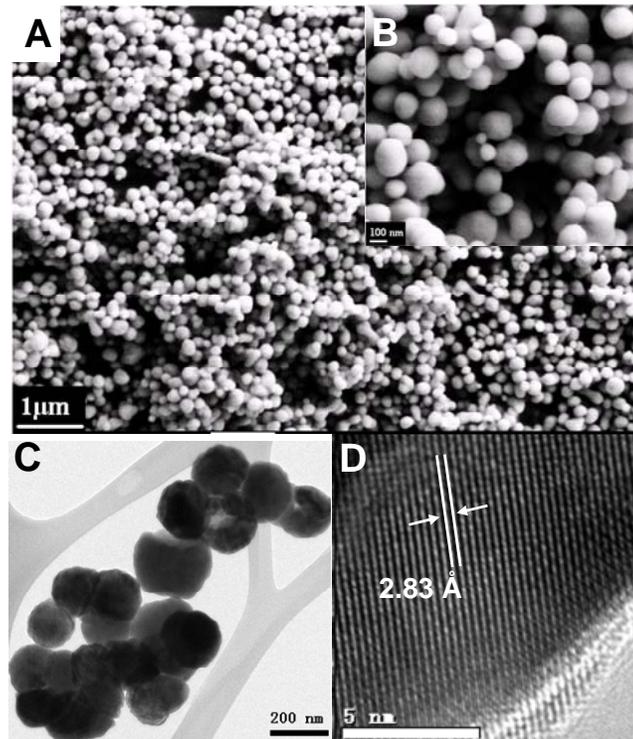
Fig. 3.2 (A) Low and (B) high magnification SEM images and (C) low and (D) high magnification TEM images of BaTiO₃ nanoparticles synthesized in water.
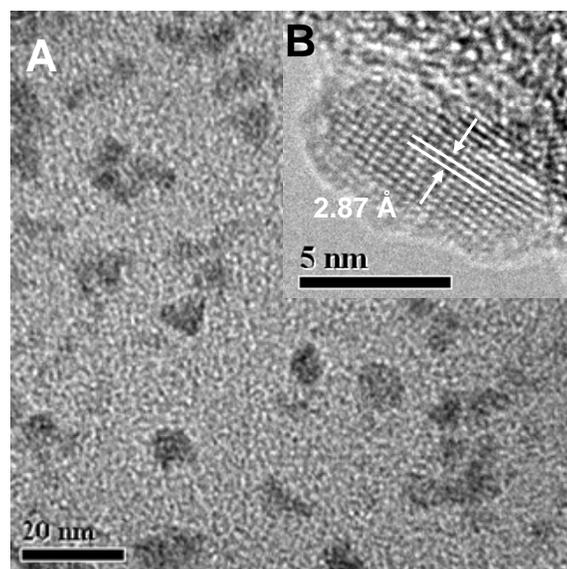
Fig. 3.3 Representative TEM images of BaTiO$_3$ nanoparticles synthesized in ethanol. (A) An overview image at low magnification; (B) high-resolution TEM images of isolated BaTiO$_3$ nanoparticles.
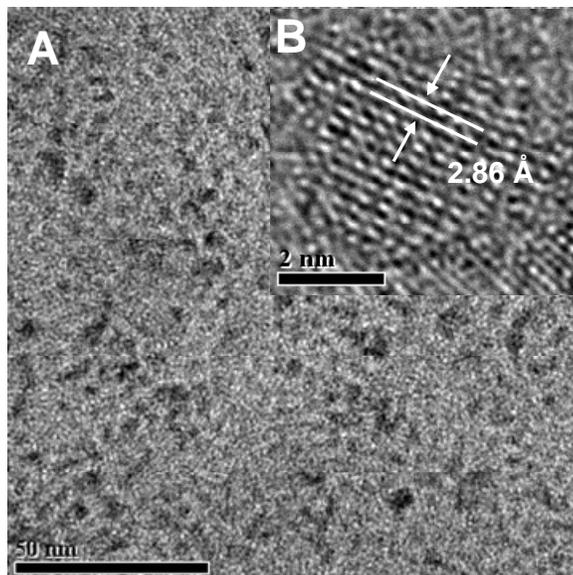
Fig. 3.4 Representative TEM images of BaTiO$_3$ nanoparticles synthesized in benzyl alcohol. (A) An overview image at low magnification; (B) high-resolution TEM images of isolated BaTiO$_3$ nanoparticles.

Images of isolated nanocrystals at higher magnification (Fig. 3.2D, 3.3 B and 3.4B) show sets of lattice fringes, giving additional evidence that the particles are highly crystalline. The measured d-spacings are labeled in the figures, which are 2.83, 2.87 and 2.86 Å for nanoparticles synthesized in water, ethanol and benzyl alcohol, respectively. Considering their related structures, the d-spacing values of both cubic and tetragonal BaTiO$_3$ phases are very

close. The d-spacing of (110) plane is 2.85 Å for cubic symmetry and 2.825 Å for a tetragonal phase. However, nanocrystals may have a variation in lattice parameters in TEM measurements, and it is difficult to conclusively assign the calculated d-spacing to a certain phase, considering the deviation from measurements as well as the difficulties in distinguishing the two similar structures. Kolen'ko and coworkers[72] performed the selected area electron diffraction (SAED) to identify the structure, but the weakly resolved rings did not allow for a clear identification, although the d values tend to a tetragonal P4mm space group over the cubic one. Therefore, further characterization is still needed for the phase determination besides TEM measurements.

3.3 Formation Mechanism and Solvent Effect

In the preparation of BaTiO$_3$ nanocrystals, the effects of reaction conditions such as temperature, reaction time, precursor concentration, liquid volume filled in the bomb and addition of surfactants were all explored. Among them, the composition of solvents seems to play an essential role in determining the size of the particles, consistent with some previous reports using similar methods.[18, 72, 74, 75]

Scheme 3.1 presents a simplified reaction mechanism including three steps. The dissolution of metallic barium in benzyl alcohol prior to the addition of the metal alkoxide is shown in step 1. A C-C bond was subsequently formed between the isopropoxy ligand of titanium isopropoxide and benzyl alcohol, through a sophisticated pathway proposed by

Niederberger *et al.*[33] The final titanium metal oxide in step 2 was promoted by the release of the hydroxyl group from benzyl alcohol and another release of 4-phenyl-2-butanol. The two alkoxide compounds of barium and titanium obtained in Step 1 and 2 then form a netlike bimetallic alkoxide precursor containing M-O-M bonds (M = Ti, Ba), which can decompose during the heating procedure, resulting in $BaTiO_3$ nanocrystals.[76]

Scheme 3.1 Simplified reaction mechanism for the formation of $BaTiO_3$[33, 76, 77]

Step 1:

$$Ba\ (s) + 2\ C_6H_5CH_2OH \rightarrow Ba^{2+} + 2\ C_6H_5CH_2O^- + H_2$$
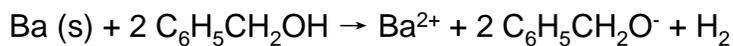
Step 2:
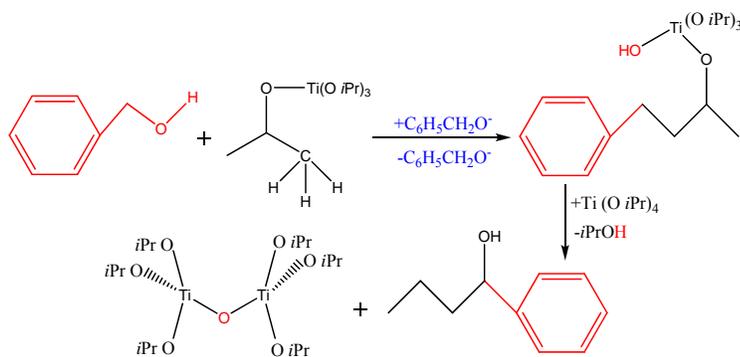
Step 3:
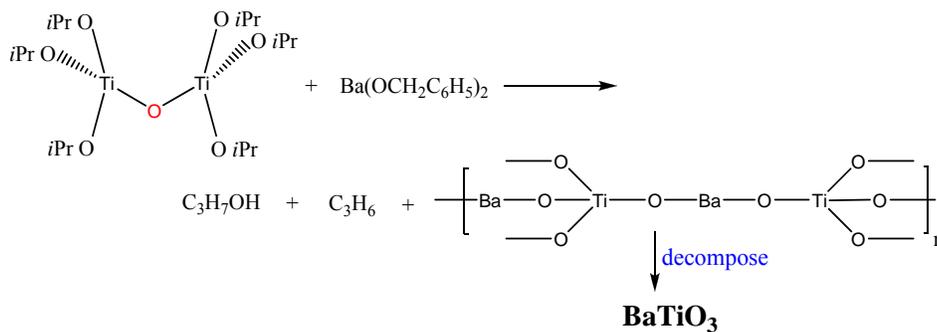
The size of nanocrystals prepared by hydrothermal and solvothermal reactions is determined by the balance between particle nucleation and growth.[18] In principle, small crystallites tend to rapidly dissolve, and the dissolved ions are more stable in solvents with high dielectric constants. By contrast, in solvents with low dielectric constants, saturation of ions easily occurs and small crystallites may be preferred. This accelerates the nucleation process and more nuclei are formed in the initial stage in the solvent with a low dielectric constant, resulting in the formation of small crystals.[41, 78] At room temperature, the dielectric constants of the three solvents can be compared as follows: water (80.1) > ethanol (24.3) > benzyl alcohol (13.0). Obviously, the high dielectric constant of water leads to the formation of fewer nuclei in the initial stage of crystal growth, which finally result in larger crystals compared with those synthesized in ethanol and benzyl alcohol.

On the other hand, in the reaction system, the employed water, ethanol and benzyl alcohol not only acted as solvents but also acted as capping agents,[75] which probably bounded to specific crystal surface and thus limited the crystal growth. In this case, the geometry or steric hinderance of solvents also seems to be an important factor in controlling the particle size, since molecules with larger volume on the surface of particles will prevent further reaction between these particles and suppress the growth. The effect of steric hinderance decreases in the order: phenylmethanolate > ethanolate > hydroxide. Accordingly, the capped phenylmethanolate and ethanolate on the surface of a particle passivate the surface, inhibiting particle growth and leading to smaller particle sizes than those in water.

As described above, the as-prepared $BaTiO_3$ particles through solvothermal and hydrothermal methods with different diameters are strongly dependent on the solvent composition. In comparison to the synthesis in the presence of surfactants, the solvent-controlled approaches are considerably simpler. The main advantages lie in the high purity of product and nontoxicity. Moreover, the synthesis temperature at 200 ^{o}C is notably lower than those applied in traditional methodologies, which significantly decreases probability of secondary phase formation. It is particularly important especially when dopant is introduced to the system. Generally speaking, this low temperature solvent-controlled synthesis strategy offers a promising cost-effective approach to producing crystalline $BaTiO_3$ nanoparticles with high purity and tunable sizes.

3.4 Phase Transition Investigated by Raman Spectroscopy

Along with the XRD analysis, which gives average and static symmetry, the local and dynamic symmetry of hydrothermally and solvothermally produced $BaTiO_3$ is also monitored by Raman spectroscopy. According to the selection rules, all the optical modes of $BaTiO_3$ with perfect cubic symmetry should be Raman inactive, whereas the same modes for the polarized tetragonal form should be Raman active. Therefore, Raman scattering spectroscopy is a highly sensitive spectroscopic technique to probe the local structure of atoms, and is widely used to analyze the phase of $BaTiO_3$.

In both the paraelectric and ferroelectric phases, $BaTiO_3$ has five atoms per unit cell

that results in 12 optical modes. In the cubic O_h symmetry, the 12 optical modes transform as $3T_{1u}$ (IR) + $1T_{2u}$ irreducible representations. The T_{2u} mode is silent and the T_{1u} modes are only infrared active. Consequently, no normal Raman mode exists in the paraelectric phase with ideal cubic perovskite symmetry.[73] Although the cubic phase theoretically does not reveal any Raman activity, high temperature Raman spectra, however, show the existence of two broad bands at ~ 260 and 530 cm^{-1}. This has been generally attributed to the local disorder associated with the position of Ti atoms.[79]

For C_{4v} point group related to the ferroelectric tetragonal phase, each of the T_{1u} mode splits into a doubly degenerate E mode and a nondegenerate A mode. While the T_{2u} silent mode splits into B_1 and E modes, resulting in $3A_1$(IR, R) + $1B_1$(R) + 4E(IR, R) modes. All the A_1 and E modes are both Raman and infrared active and the B_1 mode is only Raman active. Long-range electrostatic forces induce the splitting of transverse and longitudinal phonons, referred to as TO and LO, respectively. We then obtain the distinct Raman modes: $3[A_1(TO) + A_1(LO)] + 1B_1 + 4[E(TO) + E(LO)]$ for the room temperature tetragonal BaTiO$_3$ crystals.[73, 80]

Fig. 3.5 shows the Raman spectrum of BaTiO$_3$ bulk and nanoparticles prepared in water, ethanol and benzyl alcohol. The assignments at the top correspond to the Raman modes. There is a spectral dip at around 185 cm^{-1} for the bulk sample but a spectral peak for all the nanoparticles. This dip is known to appear for depolarized single crystals and polycrystalline samples at room temperature owing to the anharmonic coupling among three A_1 (TO$_1$) phonons.[79] On the other hand, the positive peak between 180 and 190 cm^{-1} usually appears for

powders prepared through the hydrothermal, sol-gel methods.[9] Shiratori et al.[73] assumed this change of coupling behavior may be caused by lattice defects in fine particles. A broad band detected around 256 cm^{-1} is assigned to the A_1 (TO_2) mode, a sharp peak at 306 cm^{-1} to E(TO + LO), B_1 modes, the asymmetric band around 515 cm^{-1} to E(TO) and $A_1(TO_3)$ modes, and the highest-frequency band around 717 cm^{-1} to E(LO), A_1(LO) phonon modes.
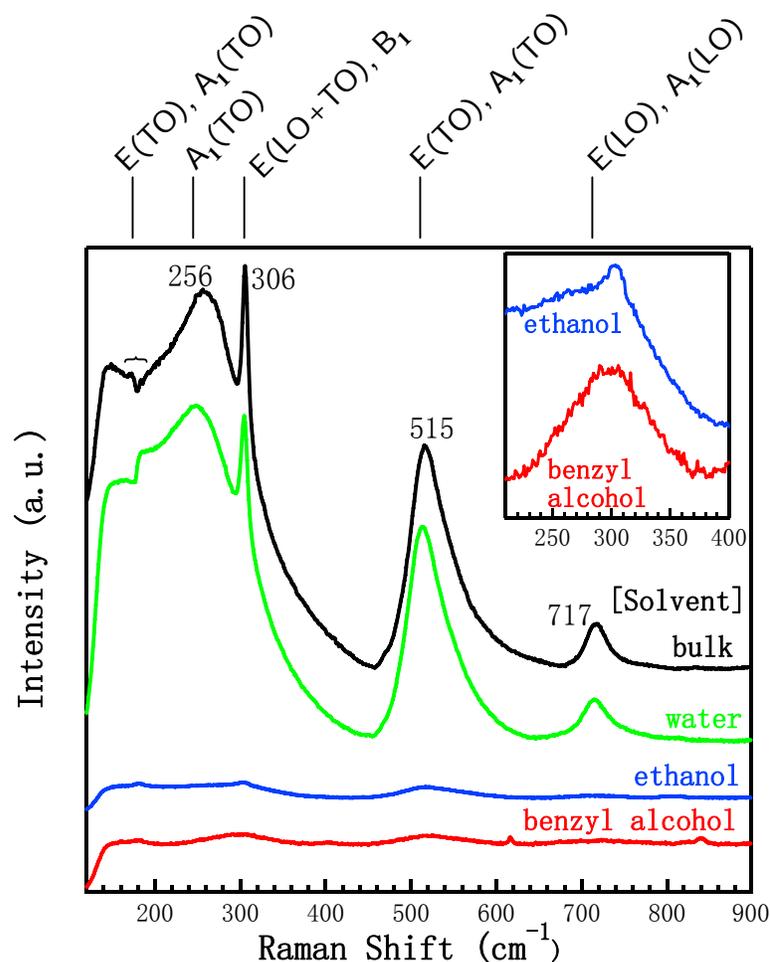
Fig. 3.5 Raman spectra of BaTiO$_3$ particles prepared in different solvents and commercial bulk BaTiO$_3$ powder for comparison. The locations of Raman modes are indicated at the top

of the figure. The inset shows the 200- 400 cm^{-1} region of particles synthesized in ethanol and benzyl alcohol.

In Raman spectroscopy, it is widely accepted that the tetragonal to cubic phase transition can be easily identified by the disappearance of the sharp mode at 306 cm^{-1} and the mode around 717 cm^{-1}.[1, 81] As shown in Fig. 3.5, in comparison with the bulk BaTiO$_3$ powder which is supposed to be tetragonal, all the phonon modes become weaker and broader with decreasing the particle size. Among them, the water-synthesized nanocrystals reveal only a little weakening and broadening of the characteristic peaks centered at 306 and 717 cm^{-1}, which gives clear evidence for the tetragonal structure in nanoparticles around 200 nm. However, the two bands decrease rapidly in the particles synthesized in ethanol and benzyl alcohol which are smaller than 10 nm, consistent with reports by others.[73] Though similar in the overall peak intensities, the expanded spectral region of ethanol- and benzyl alcohol-synthesized BaTiO$_3$ displayed in the inset of Fig. 3.5 still show notable variation of the 306 cm^{-1} line. A distinct peak at 306 cm^{-1} mixed with a broad peak is presented in the 7.5-10 nm particles synthesized in ethanol, indicating the presence of local tetragonal crystal structure. Considering that the peak is reduced in its sharpness, to what extent this tetragonality expands by long-range ordering cannot be described conclusively from the present results. It is not so surprising to observe the tetragonality in such small BaTiO$_3$ nanoparticles using Raman spectroscopy, since BaTiO$_3$ nanocrystals ranging from 20- 30 nm

were reported to have tetragonal symmetry based on Raman active modes by several groups.[18,][73] However, our observation push this size limit down to as small as 10 nm or lower. Detailed inspection of BaTiO$_3$ synthesized in benzyl alcohol with 4-5 nm in diameter shows the disappearance of the 306 cm^{-1} sharp line when the tetragonal phase is not dominant. However, it is worth noting that a mixture of Raman scattering features can be observed at around 297, 515 and 720 cm^{-1} in this benzyl alcohol synthesized powder (a scaled graph is shown in Fig. 4.7), which is not expected from group selection rules for the ideal cubic symmetry. Shiratori *et al.*[73] attributed this to a mixture of a dominant cubic and a very minor tetragonal portion since the intensity of the tetragonal features is very low, which agrees with the XRD analysis discussed previously.

There are some impurities existing in the systems, particularly with the small particles due to defects and stress in the lattice. Below 200 cm^{-1}, some weak scattering is due to a BaCO$_3$ impurity. Features around 630 cm^{-1} may correspond to BaCO$_3$ phase, anatase TiO$_2$, or hexagonal BaTiO$_3$ which can be stabilized at room temperature by high surface energy.[2, 9, 73] All those impurities are commonly seen in the Raman spectrum of BaTiO$_3$ nanoparticles, and assignments are still under discussion in literature. In addition, a mode at ~ 815 cm^{-1} is due to the hydroxyl absorbed on the nanoparticle boundary,[20] which is usually observed in nanoparticles through hydrothermal or solvothermal reactions.

Generally speaking, as the size decreases in the as-prepared BaTiO$_3$ nanocrystals controlled by solvents, the tetragonality degree interpreted by the observed intensity of

characteristic peaks centered at 306 cm^{-1} is decreased gradually, showing a size effect on the crystal structure. In a local and dynamic point of view of symmetry, BaTiO$_3$ nanoparticles around 200 nm synthesized in water is predominantly tetragonal; nanocrystals synthesized in ethanol of 7.5-10 nm remain tetragonal though weakened, while the benzyl alcohol synthesized powder as small as 4-5 nm have a majority of cubic symmetry with a minor tetragonal portion caused by the local disorder associated with the position of Ti atoms.

Chapter 4   Study of Cr^{3+}-Doped $BaTiO_3$ Nanocrystals

4.1 Phase Transition in Water-Synthesized $BaTiO_3$ Nanocrystals

Cr^{3+}-doped $BaTiO_3$ nanocrystalline particles were synthesized in water with different starting concentrations of Cr^{3+}. As mentioned in Chapter 2, two methodologies were employed in the water synthesized particles, because the dopant precursor $Cr(acac)_3$ does not dissolve in water as it does in ethanol and benzyl alcohol, which significantly decreased the dopant concentration in the final products. In order to enhance the incorporation of Cr^{3+} dopant ions, besides the employment of $Cr(acac)_3$ denoted as **method A**, $CrCl_3 \cdot 6H_2O$ was also added after dissolution in water, labeled as **method B**. The starting molar ratio of Cr^{3+} to Ti^{4+} was varied from 0 to 0.15.

XRD patterns of nanocrystals with starting dopant concentration at 5%-A, 15%-A, 5%-B and 8%-B, as well as undoped and bulk $BaTiO_3$ are presented in Fig. 4.1A. Similar to the pure $BaTiO_3$ nanoparticles synthesized in water, all Cr^{3+}-doped powders reveal a highly crystalline $BaTiO_3$ feature without any byproducts or secondary phase. The sizes of doped particles remain the same as those of pure $BaTiO_3$ synthesized in water as evidenced by unchanged peak broadening. The effect of dopant in crystal size is negligible in this size regime. Doping a crystal results in gradual shifts in the lattice parameters. The shifts arise from the strain induced by substituting the host ions with dopants. To give a clear view of this observation, enlarged patterns between 44.0º and 46.5º are shown in Fig 4.1B. As expected, the peaks in

this region keep shifting to lower angle from the undoped to 5%-A, 15%-A, 5%-B and 8%-B particles, indicating that the dopant incorporation into the BaTiO$_3$ crystal lattice increases in the same order, and **method B** does introduce more dopant to the lattice than **method A**. In fact, if the actual doping concentration into the host lattice was determined, the average lattice parameter should have varied linearly with dopant concentration, known as Vegard's law.[82] Deviations from linearity are indications of phase transition or segregation.
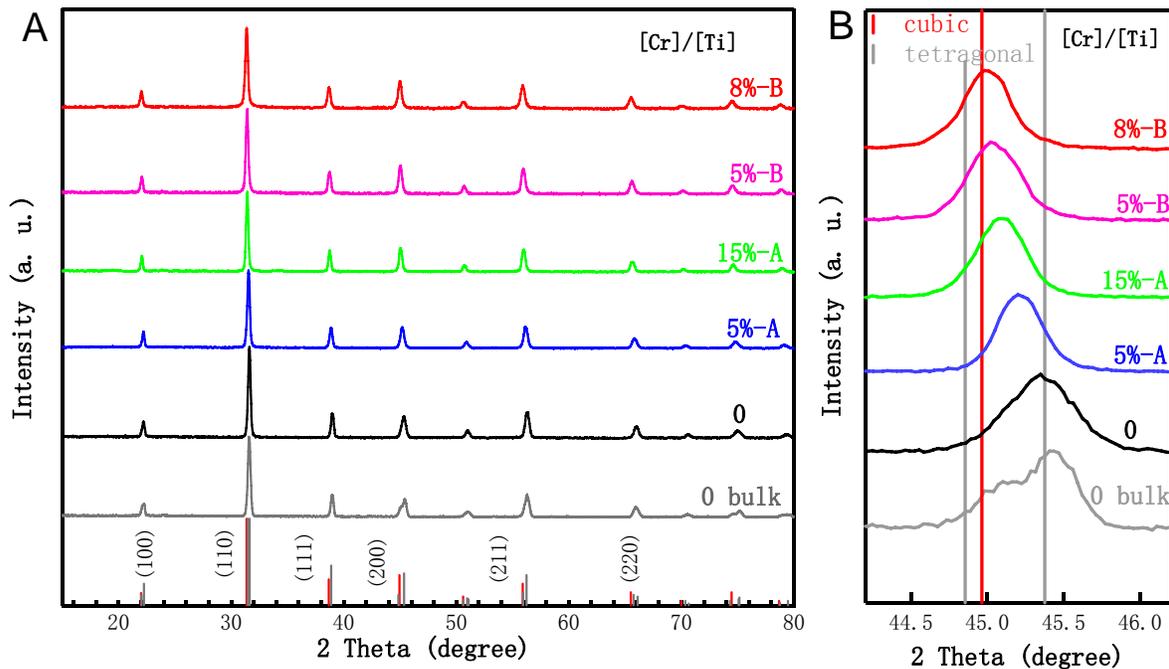
Fig. 4.1 (A) XRD patterns of Cr^{3+}-doped BaTiO$_3$ nanocrystals synthesized in water with different Cr^{3+}/Ti^{4+} molar ratios (top to bottom): 8%-B, 5%-B, 15%-A, 5%-A, 0 and commercial bulk BaTiO$_3$ powder for comparison. A and B correspond to different doping methods. The vertical lines represent the standard patterns of bulk cubic-BaTiO$_3$ (red) and tetragonal-BaTiO$_3$ (grey); (B) Enlarged XRD patterns between 44.0^o and 46.5^o.

When Cr^{3+} is induced to $BaTiO_3$ lattice, it prefers to substitute at the Ti^{4+} site with oxygen vacancy compensation,[51] due to their similar ionic radii in octahedral coordination ($r(Cr^{3+})$ = 0.62 Å, $r(Ti^{4+})$ = 0.61 Å). In this case, the trivalent Cr^{3+} behaves as an acceptor. However, when the tetravalent Ti^{4+} ions are substituted by a trivalent foreign ion, the Ti-O attractive interaction which helps to stabilize the $BaTiO_3$ lattice may be weakened. As a result, the lattice will expand to some extent. This may be one of the reasons why the XRD reflections shift to lower angles. However, such small doping concentration cannot account for XRD shift simply through Vegard's law. As indicated by the vertical lines representing standard patterns of bulk $BaTiO_3$ in Fig. 4.1, the lower angle shifts exactly correspond to a phase transition from tetragonal to cubic symmetry. Starting from the undoped $BaTiO_3$ nanocrystals centered around the tetragonal (200) line, a dramatic shift occurs to 5%-A with the lowest doping concentration, and all the other doped nanoparticles reveal a clear shift to the cubic (200) pattern. Finally the XRD pattern of highly doped 8%-B matches the cubic phase. As we concluded in Chapter 3, $BaTiO_3$ nanocrystals synthesized in water exhibit a manifest tetragonal signal both in XRD and more obviously in Raman spectra, though notable splitting of (200) peak was not observed as it is in bulk material. Here, in comparison with the Cr^{3+}-doped $BaTiO_3$ nanoparticles which undergo a lattice expansion together with a cubic-to-tetragonal phase transition, the existence of tetragonality in undoped $BaTiO_3$ is further proved. In addition, if we take the 8%-B Cr^{3+}-doped $BaTiO_3$ as an example, an asymmetric (200) peak is observed in this highly doped sample, indicating a shifted tetragonal

symmetry or more probably a mixture of both the cubic and tetragonal phases.

Generally speaking, XRD measurement provides an average and static structure of Cr^{3+}-doped $BaTiO_3$ nanoparticles synthesized in water. Undoped $BaTiO_3$ nanocrystals are confirmed to have a majority of tetragonal form, and this tetragonal signal is decreased gradually as more dopants are induced into the lattice, which expand the lattice parameters, and shift the (200) peak to 2θ values typical at the cubic phase. However, it seems that there still remains some tetragonality even in the highly doped nanocrystals, which can be further investigated by Raman spectroscopy.

Displayed in Fig. 4.2 are Raman spectra for the pure and Cr^{3+}-doped $BaTiO_3$ nanoparticles synthesized in water. Each peak observed can be assigned to a tetragonal $BaTiO_3$ optical mode, and almost no impurities or defects are detected. Consistent with the XRD results, the tetragonal signal is gradually suppressed with introduction of more dopant ions, exhibiting weaker peak intensity and broader peak width. However, some tetragonal features still remain in the highly doped nanocrystals 5%-B and 8%-B, as the existence of a weak but cognizable peak at 304 cm^{-1} (inset of Fig. 4.2), which is attributed to the E(LO+TO), B_1 modes. This is also in good agreement with the asymmetric peak in XRD patterns.
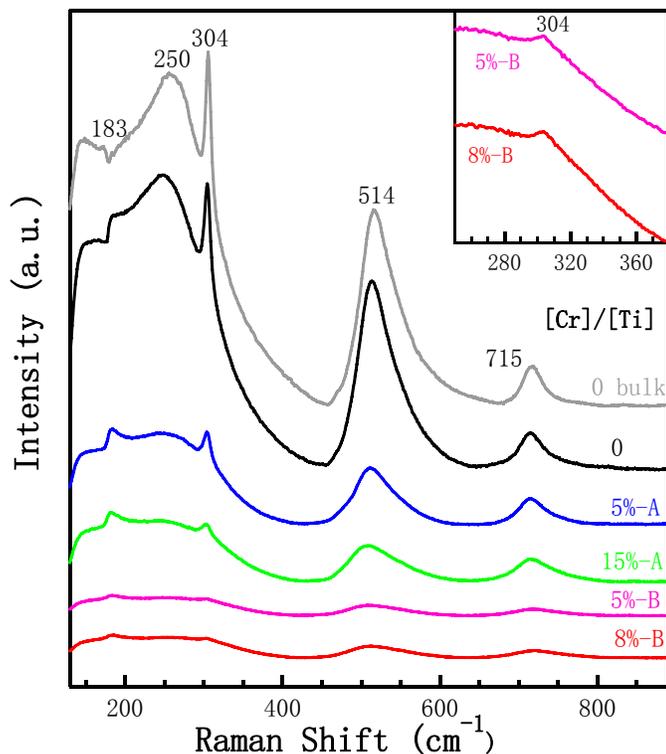
Fig. 4.2 Raman spectra of BaTiO$_3$ nanocrystals prepared in water with different Cr^{3+}/Ti^{4+} molar ratios (bottom to top): 8%-B, 5%-B, 15%-A, 5%-A, 0 and commercial bulk BaTiO$_3$ powder for comparison. The inset shows an enlarged 304 cm^{-1} peak of nanocrystals with Cr^{3+}/Ti^{4+} ratios 5%-B and 8%-B.

We interpret the disappearance of the 304 cm^{-1} and 715 cm^{-1} peaks as an indicator of the decrease of tetragonal phase degree and use the linewidths of these two peaks to probe the phase evolution.[18, 25] The linewidth of 304 cm^{-1} peak was obtained by subtracting a sloping baseline curve.[83] Shown in Fig. 4.3A and B, the linewidths of both peaks increase, from bulk to nanosized BaTiO$_3$ synthesized in water, further to Cr^{3+}-doped nanocrystals. The much larger linewidths in Raman peaks of the highly doped nanoparticles suggest that the

tetragonality present is accompanied by a significantly decreased structural stability. The linewidth analysis shows a clear evidence of the tetragonal-to-cubic phase evolution induced by dopant ions.
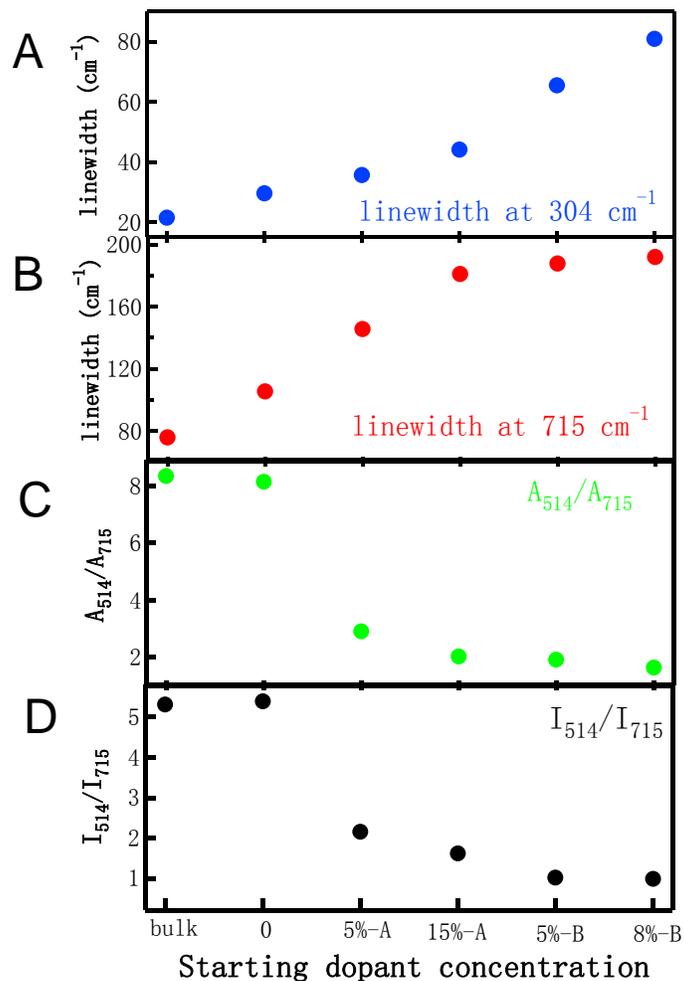
Fig. 4.3 Results from the Raman data of BaTiO$_3$ nanocrystals synthesized in water with different Cr^{3+}/Ti^{4+} molar ratios and commercial bulk BaTiO$_3$ powder. Linewidth of the (A) 304 cm^{-1} and (B) 715 cm^{-1} as a function of doping concentration; Dependence of the ratio of (C) peak integration area and (D) peak intensity at 514 cm^{-1} to 715 cm^{-1} upon the doping concentration.

Although both XRD and Raman measurements suggest the same trend of the doping concentration, consistent with the starting percentage of the precursor, further detailed values of the incorporation of dopant into the lattice obtained by other characterization technique such as inductively coupled plasma (ICP) will quantitatively provide the effect of dopants on the $BaTiO_3$ structures, which might lead to a better understanding of the doping and phase transition mechanism.

In the Raman spectra shown in Fig. 4.2, it is also interesting to compare the higher relative intensity of the band at 715cm^{-1} with the other tetragonal bands, regarding to the different Cr^{3+}/Ti^{4+} molar ratio. According to reports by Urban et al.,[84] the Raman spectrum of $BaTiO_3$ is also sensitive to the change of Ba/Ti stoichiometry. Busca[85] claimed that the intensity of the peak at 715 cm^{-1}, with respect to that at 514 cm^{-1}, takes a minimum when Ba/Ti equals 1. Otherwise the band grows when either Ba or Ti is in excess. The ratio of peak intensities at 514 and 715 cm^{-1} (I_{514}/I_{715}), as well as the ratio of peak integration area (A_{514}/A_{715}) are plotted as a function of the supposed doping concentration (Fig. 4.3D and 4.3C). The ratios of both bulk and undoped $BaTiO_3$ synthesized in water reveal a high number, suggesting that the undoped 200 nm $BaTiO_3$ nanoparticles have more balanced Ba/Ti composition in comparison with the doped nanoparticles. These ratios decrease with increasing presence of the dopant ions. This agrees well with the chemistry in the doping system, since Ba/Ti ratio changes when the Ti^{4+} is substituted by the transition metal Cr^{3+} ions. It indirectly indicates the successful doping with different concentrations. The origin of the

spectral parameter changes has not been completely understood yet. It is believed, however, that disorder introduced by point defects such as oxygen vacancies can subtly change the polarizability and therefore Raman band intensities and shapes.

4.2 Phase Transition in Ethanol-Synthesized BaTiO$_3$ Nanocrystals

The phase transition behavior of ethanol-synthesized Cr^{3+}-doped BaTiO$_3$ nanocrystals is investigated in the same way as those in water. The starting Cr^{3+}/Ti^{4+} ratios are specified at 5%, 10%, 15% and 20%, using consistent doping methodology. Typical XRD patterns are presented in Fig. 4.4. Except some orthorhombic BaCO$_3$ detected in the 20% Cr^{3+} highly doped powder, all the other nanocrystals seem well crystallized and almost pure. No obvious broadening of peaks was observed compared with the undoped BaTiO$_3$ crystals, indicating the dopants effect on particle size is not considerable in this system. The Debye-Scherrer equation gives a diameter ranging from 6-8 nm. The expanded (200) line which characterizes the phases in XRD is shown in Fig. 4.4B. Similar to the shifts detected in the water system, the (200) patterns here are shifted to lower angle in all the Cr^{3+}-doped nanocrystals, indicating that the dopant expands the crystal lattice and promotes the tetragonal-to-cubic phase transition. Although not as notable as those in samples prepared in water due to the difficulties in accessing crystal structures for particles as small as 10 nm, slight shifts are still discernable between different doping levels.
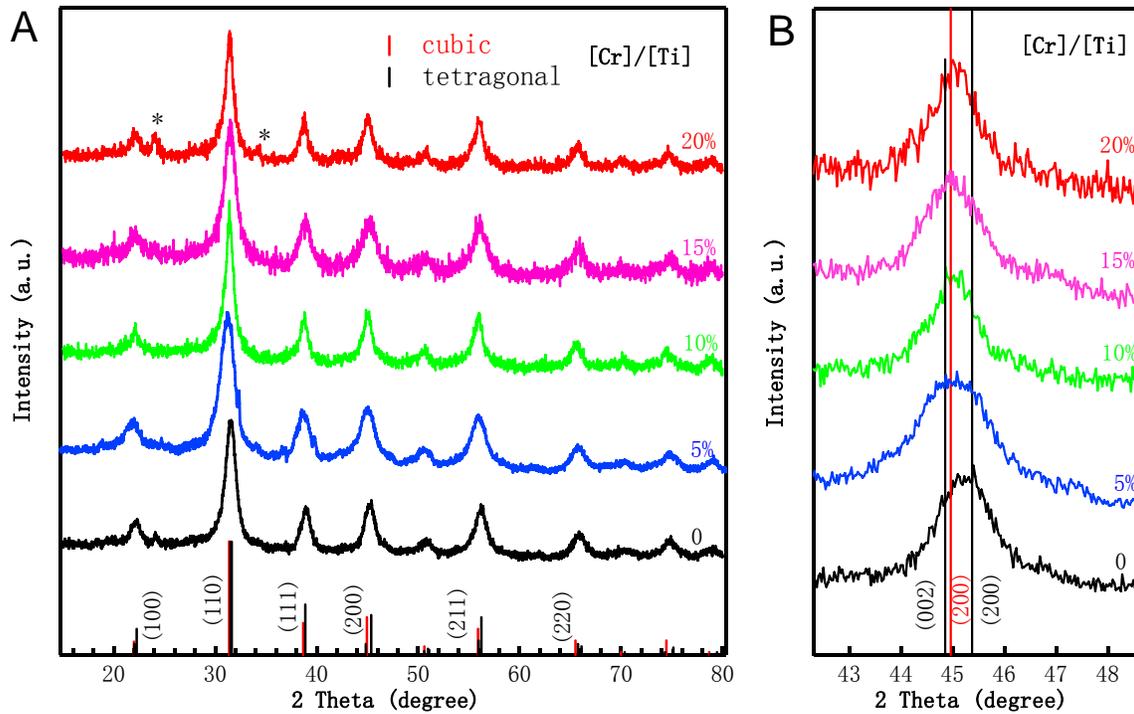
Fig. 4.4 (A) XRD patterns of Cr^{3+}-doped $BaTiO_3$ nanocrystals synthesized in ethanol with different Cr^{3+}/Ti^{4+} molar ratios (top to bottom): 20%, 15%, 10%, 5% and 0. The vertical lines represent the standard patterns of bulk cubic-$BaTiO_3$ (red) and tetragonal-$BaTiO_3$ (black). * corresponds to orthorhombic $BaCO_3$; (B) Enlarged XRD patterns between 42.0^o and 49°.

Following XRD, Raman spectroscopy has been used to characterize the phase evolution. As displayed in Fig. 4.5, main bands centered at 180, 300, 517 and 715 cm^{-1} are attributed to $[E(TO), A_1(TO)]$, $[E(LO+TO), B_1]$, $[E(TO), A_1(TO)]$ and $[E(LO), A_1(LO)]$ modes, respectively. As expected, decrease in the contribution of the tetragonal structural stability is accompanied by the larger linewidth and lower intensity of peaks in the Cr^{3+}-doped nanocrystals. In the 20% doped particles the characteristic peak at 300 cm^{-1} is almost lost, and

the peak around 715 cm^{-1} is flattened, which further confirms the quenching of ferroelectric phase by Cr^{3+} dopants.
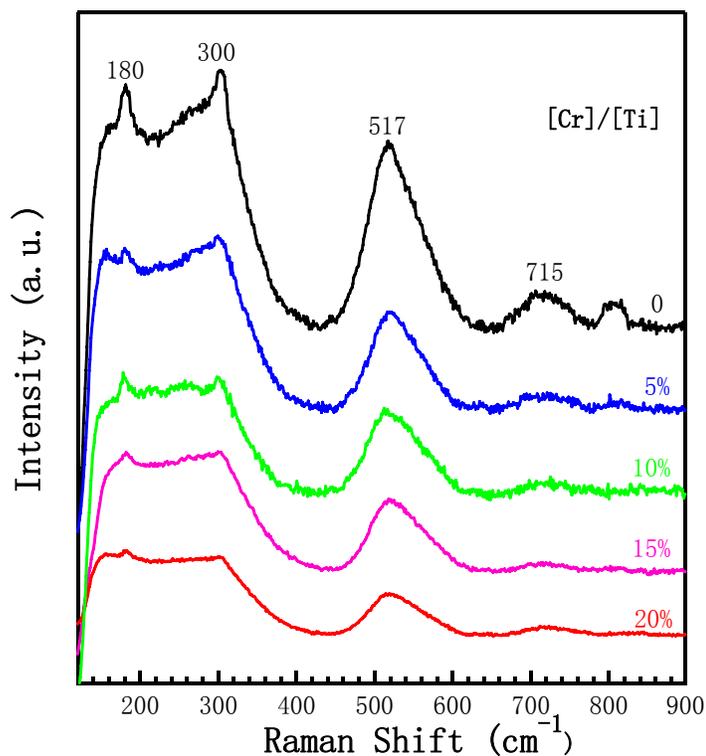
Fig. 4.5 Raman spectra of BaTiO$_3$ nanocrystals prepared in ethanol with different Cr^{3+}/Ti^{4+} molar ratios (bottom to top): 20%, 15%, 10%, 5% and 0.

It is interesting to note that a bump centered around 800 cm^{-1} in the undoped BaTiO$_3$, which is an indication of hydroxyl defects on the surface, is not showing up in all the Cr^{3+} doped samples. Therefore it is supposed that by introducing foreign ions, the surface adsorbed hydroxyl group can be removed in this ethanol-synthesized system. One of the possible reasons is the charge compensation induced by dopants. With the disappearance of the

hydroxyl group, the tetragonality is not stabilized but instead lessened because of dopants. This leads to the conclusion that the defects especially OH⁻ group are not an intrinsic source of the tetragonal-to-cubic phase transformation (possible factors are discussed in Chapter 1), at least in this size region. Also, the intensity ratios of I_{517}/I_{715} which are associated with the Ba/Ti ratio do not vary significantly. We attribute this to the flattening of the 715 cm⁻¹ band.

4.3 Phase Transition in Benzyl Alcohol-Synthesized BaTiO₃ Nanocrystals

When the BaTiO₃ grain size is decreased further, the tetragonality is suppressed and cubic becomes the dominant symmetry as discussed in Chapter 3. In this sense, probing the phase transition is even more challenging.

XRD patterns of Cr³⁺-doped BaTiO₃ nanocrystals (Fig. 4.6) indicate again the crystalline domain sizes of 4-5 nm. Closer inspection in Fig 4.6B reveals detailed structural information of those small particles. Tetragonality does exist somehow in the pure BaTiO₃ synthesized in benzyl alcohol, since the Cr³⁺ doped nanocrystals crystals prepared in the same condition are losing the tetragonal splitting and peak position by shifting to lower angles. In fact, the 5% and 10% Cr³⁺-doped nanoparticles still exhibit a tiny amount of asymmetry of the (200) peak, while the 20% doped ones seem to completely match the cubic standard line. However, this is not conclusive evidence owing to the extensive peak broadening and the subtle changes in the peak shape. Actually, even existing in those small particles, tetragonal form should not be the major phase at this scale.
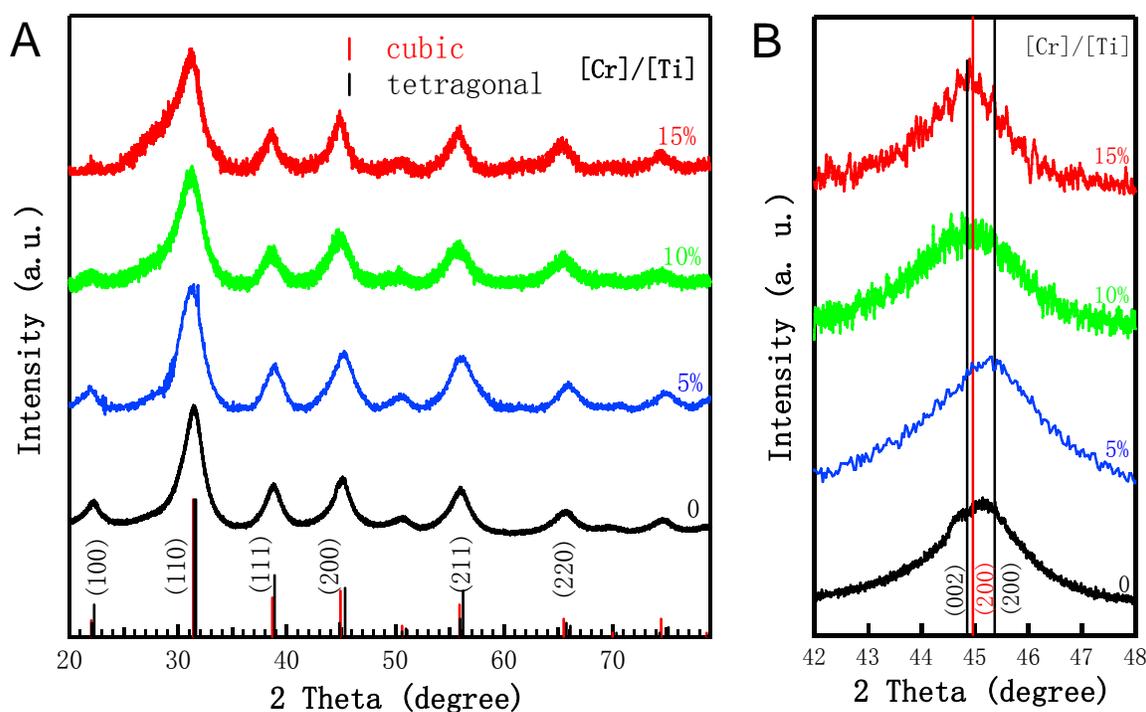
Fig. 4.6 (A) XRD patterns of Cr^{3+}-doped $BaTiO_3$ nanocrystals synthesized in benzyl alcohol with different Cr^{3+}/Ti^{4+} molar ratios (top to bottom): 15%, 10%, 5% and 0. The vertical lines represent the standard patterns of bulk cubic-$BaTiO_3$ (red) and tetragonal-$BaTiO_3$ (black); (B) Enlarged XRD patterns between 42.0° and 48°.

This assumption is further supported by Raman spectroscopy. Shown in Fig. 4.7, the observed low signal-to-noise ratio in the small nanocrystals indicates the lower crystallinity compared with larger particles. In addition to the 177, 300, 518 and 719 cm^{-1} bands related to [E(TO), A₁(TO)], [E(LO+TO), B₁], [E(TO), A₁(TO)] and [E(LO), A₁(LO)] modes, extra peaks are observed around 404, 616 and 840 cm^{-1}, most of which were not detected in nanocrystals prepared in the other two solvents. The 404 and 616 cm^{-1} bands can be assigned to $BaCO_3$

phase, anatase TiO_2, or hexagonal $BaTiO_3$. We note, however, that the 616 cm^{-1} peak is relatively sharp, which is not expected in the nanosized particles. The 840 cm^{-1} band is assigned again to the hydroxyl defects. Besides all the impurities in Raman spectroscopy, the remaining broad bands are due to a local disorder of Ti atoms in a relatively cubic lattice (discussed in Chapter 3) are consistent in shapes and intensities with both the pure and doped small $BaTiO_3$ nanocrystals. Because of the low degree of tetragonality in the undoped sample, the effect of dopants on phase transition is not detectable so that the intensity and shape of the broad peaks remain unchanged. Last, note the relatively higher intensity of the 719 cm^{-1} band in all the samples, which may indicate a Ba- or Ti-rich surface environment related to defects not only in the Cr^{3+}-doped $BaTiO_3$, but also for pure $BaTiO_3$ nanocrystals around 4-5 nm.
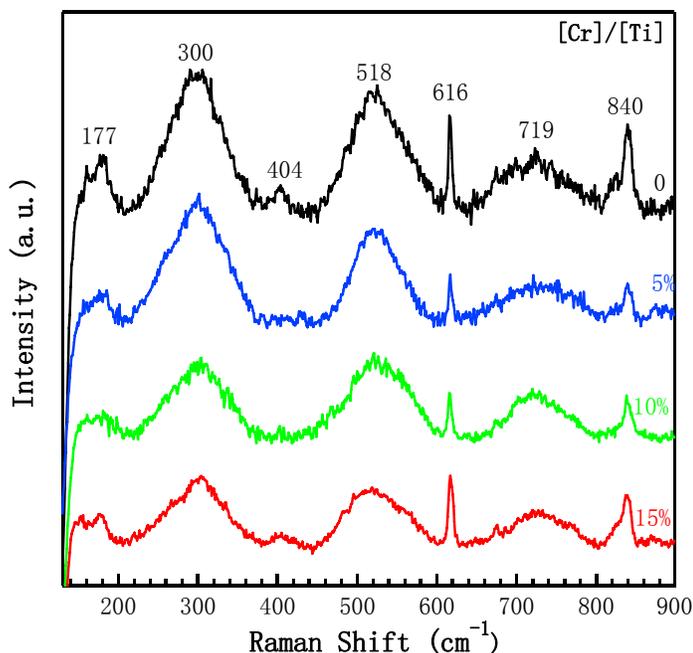
Fig. 4.7 Raman spectra of $BaTiO_3$ nanocrystals prepared in benzyl alcohol with different Cr^{3+}/Ti^{4+} molar ratios (bottom to top): 15%, 10%, 5% and 0.

4.4 UV-Vis Absorption Spectroscopy

4.4.1 Effect of Surfactants

Fig. 4.8A shows a typical electronic absorption spectrum of colloidal 15% Cr^{3+}-doped BaTiO$_3$ nanocrystals synthesized in benzyl alcohol. Two transitions are revealed at ~15850 cm^{-1} and ~23200 cm^{-1}, which can be assigned to the $^4A_{2g} \rightarrow ^4T_{2g}$ and $^4A_{2g} \rightarrow ^4T_{1g}(F)$ ligand-field transitions, respectively, of pseudo-octahedral Cr^{3+} coordinated with six O^{2-} ions, indicating the successful internal substitution of octahedral Ti^{4+} with Cr^{3+}. The $^4A_{2g} \rightarrow ^4T_{1g}(F)$ transition is observed as a shoulder due to tailing of the solvent toluene into the visible region. Very similar octahedral Cr^{3+} transition energies at 16400 cm^{-1} and 23250 cm^{-1} were observed for the analogous transition in Cr^{3+}: TiO$_2$.[67]
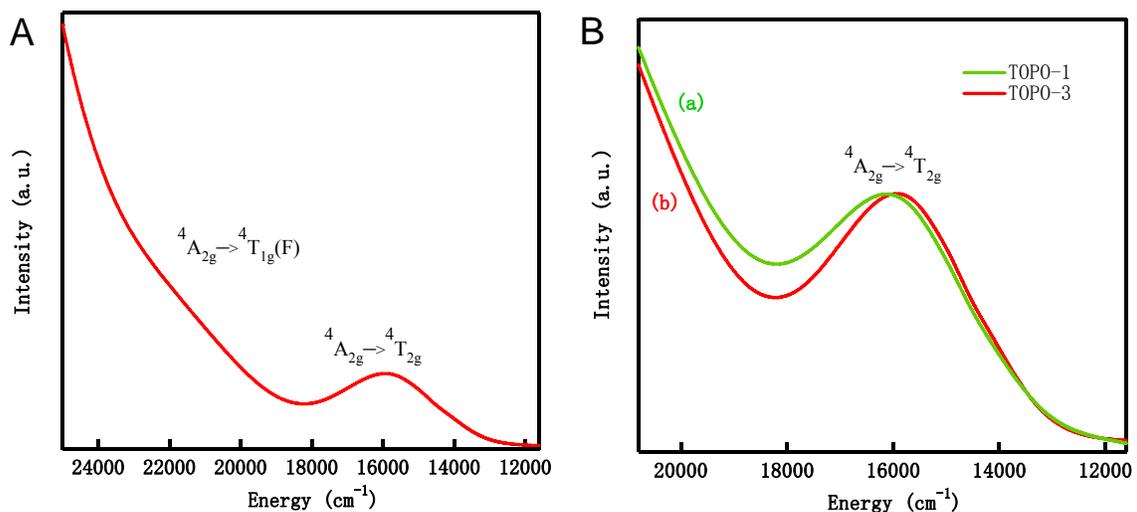
Fig. 4.8 Absorption spectra of (A) Cr^{3+}-doped BaTiO$_3$ nanocrystals synthesized in benzyl alcohol (B) the same sample treated in TOPO for (a) once and (b) three times.

The surfactant TOPO was reported to be capable of removing dopant ions from the surface of diluted magnetic semiconductor nanocrystals by complexation.[66, 86] The surface cleaning also occurred in our system. As shown in Fig. 4.8B, the $^4A_{2g} \rightarrow {}^4T_{2g}$ transition shifts ~200 cm^{-1} when the doped nanocrystals were treated once and three times with TOPO. This slight shift detected by absorption spectroscopy is actually an indication of a subtle change in the octahedral Cr^{3+} environment. The absorption band stopped changing when the sample was treated by TOPO three times, suggesting that the majority if not all of the surface bound Cr^{3+} ions were removed by using TOPO purification procedure.
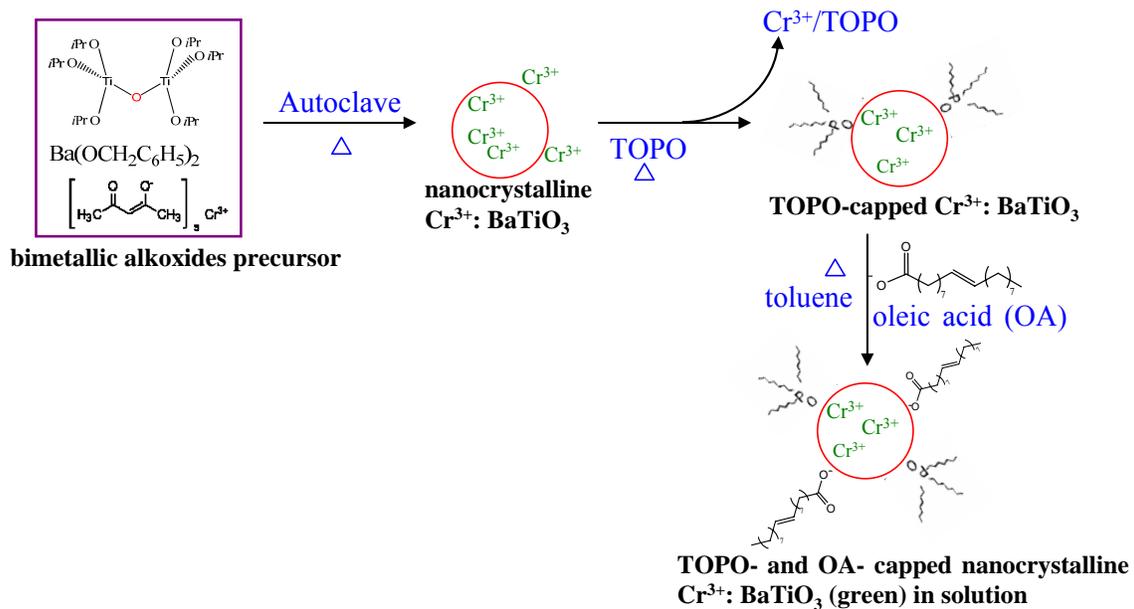
Scheme 4.1 Synthesis and surfactant functionalization of Cr^{3+}-doped BaTiO$_3$ nanocrystals

In order to obtain a colloidal suspension, various dispersants such as polyelectrolytes,

phosphate esters and fatty acids were employed for BaTiO$_3$ nanocrystals. Among them, oleic

acid proved to be the best. The benzyl alcohol- and water-synthesized nanoparticles are

dispersed well in toluene, but those prepared in water precipitated because of their relatively

larger size. We believe the repulsive force which helps to reduce the van der Waals force of

interparticle attraction and stabilize the colloidal suspensions is introduced through steric

stabilization in this case. With a carboxylic acid end group adsorbing strongly on the particle

surface, oleic acid consists another part, the essentially nonpolar hydrocarbon chain which can

protrude into the solvents. Also, oleic acid has higher packing density than TOPO,[86] resulting

in better dispersibility of BaTiO$_3$ nanoparticles. The colloidal processing of BaTiO$_3$

nanocrystals not only allows precise spectroscopic measurements, but also leads to higher

average packing densities and finer pore size distributions which are of significant industrial

importance.[4] The synthesis and purification procedures are summarized in Scheme 4.1.

4.4.2 Ligand-Field Transition in Different Systems

Investigation of the octahedral Cr^{3+} ligand-field transition can also provide a deeper

understanding of the phase transition of BaTiO$_3$ upon the particle size. The $^4A_{2g} \rightarrow {}^4T_{2g}$

absorption bands of ethanol- and benzyl alcohol-synthesized nanocrystals with different

starting doping concentration are displayed in Fig. 4.9A and B, respectively. Table 4.1

presents the peak position. It is found that the level of dopant incorporation does not influence

the absorption very much, since the bands are centered at ~16350 cm^{-1} in the ethanol system

and ~15900 cm^{-1} in the benzyl alcohol system. It is not surprising because the phase evolution induced by dopants is so weak at this size region, especially for the 4-5 nm benzyl alcohol-synthesized crystals, that obvious changes in the Cr^{3+} environment are not expected.
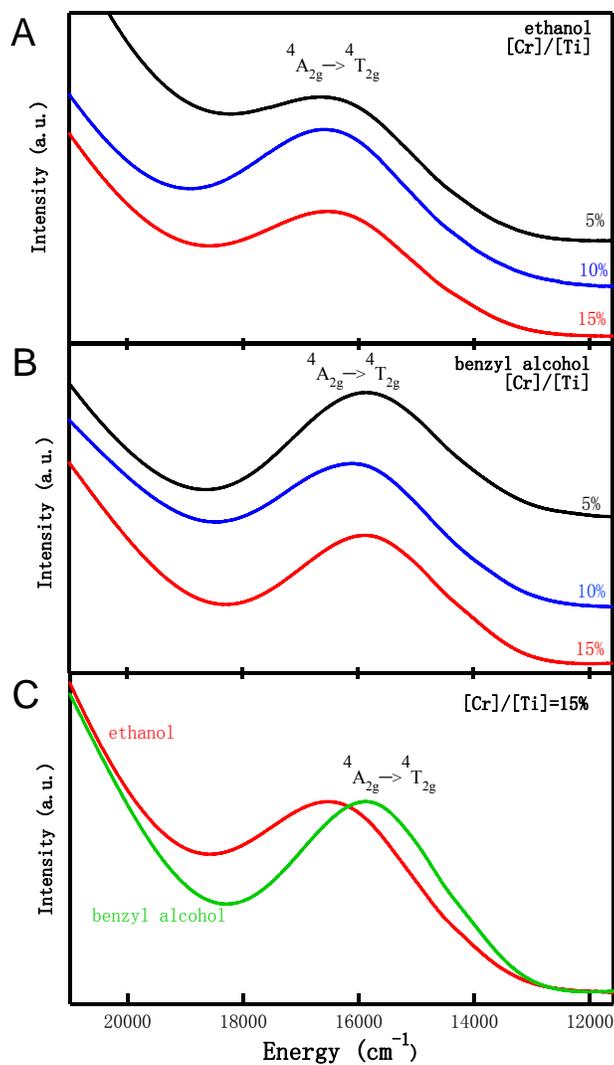
Fig. 4.9 Absorption spectra of Cr^{3+}-doped BaTiO$_3$ nanocrystals with different Cr^{3+}/Ti^{4+} molar ratios synthesized in (A) ethanol and (B) benzyl alcohol; (C) Comparison of Cr^{3+}-doped BaTiO$_3$ ([Cr]/[Ti]=15%) synthesized in ethanol and benzyl alcohol.

Table 4.1 Comparison of $^4A_{2g} \rightarrow\ ^4T_{2g}$ absorption of Cr^{3+}-doped $BaTiO_3$ nanocrystals with different Cr^{3+}/Ti^{4+} molar ratios synthesized in ethanol and benzyl alcohol.

Solvents	5%	10%	15%
Ethanol (cm^{-1})	16315	16420	16355
Benzyl alcohol (cm^{-1})	15875	16000	15810

However, the size dependence of the absorption is observed between the two systems of different solvents. As an example, consider 15% Cr^{3+}-doped $BaTiO_3$. The spectra of this sample prepared in ethanol and benzyl alcohol are presented in Fig. 4.9C. A red shift of ~550 cm^{-1} for benzyl alcohol with respect to the ethanol system suggests a significant structural change on the crystal lattice. As concluded previously, the 4-5 nm nanocrystals synthesized in benzyl alcohol possess a larger portion of cubic symmetry and a volume expansion compared with those synthesized in ethanol. The absorption spectra are sensitive to the Cr-O bonding and therefore should strongly depend on the lattice symmetry. Although experimental atom-atom distances of doped $BaTiO_3$ nanocrystals are still lacking, reports have demonstrated that the bond lengths of Ti-O, Ba-O and Ba-Ti in pure $BaTiO_3$ extend with decreasing particle size and increasing electrostatic repulsion.[18, 87] With the extension of atom-atom distance, the ligand-field strength is weakened at the same time. Therefore, similar to Ti-O bonding, the Cr-O distance is also increased at smaller particle size, which decreases the ligand-field strength and leads to the red shift of Cr^{3+} ligand-field transition of particles

synthesized in benzyl alcohol. This is another reasonable proof for the structural change and phase transition in BaTiO$_3$ nanocrystals. This dependence of Cr^{3+} ligand-field transition on nanoparticle structures will be better demonstrated and understood if it can be investigated in the water synthesized nanoparticles, where more obvious phase evolution occurs.

4.5 Comparison of Size and Dopant Effects on Phase Transition

So far, two effects that promote the tetragonal-to-cubic phase transition in BaTiO$_3$ at room temperature have been presented; size and dopant effects. The dopant species is also demonstrated by absorption spectroscopy. Thus it is worth to compare the two effects in one system. Among all the nanocrystals synthesized, pure BaTiO$_3$ prepared in water exhibits the highest tetragonal signal. Two samples are chosen for comparison: ethanol-synthesized pure BaTiO$_3$ which have smaller particle size and larger 8%-B Cr^{3+}-doped BaTiO$_3$ synthesized in water which is highly doped.

Both the XRD patterns and Raman spectra are displayed in Fig. 4.10. Variation in size is obvious since the ethanol-synthesized particles are around 10 nm while water-prepared ones have a diameter of 200 nm. However, enlarged (200) peak (inset in Fig. 4.10A) reveals the remaining tetragonality in smaller crystals and a shift to cubic symmetry in the Cr^{3+}-doped larger particles, which is contradictory to the size effect. Moreover, Raman spectra confirm this difference by the much more intense peak of ethanol-synthesized samples than that of the doped BaTiO$_3$ nanocrystals at specific 303 cm^{-1}.
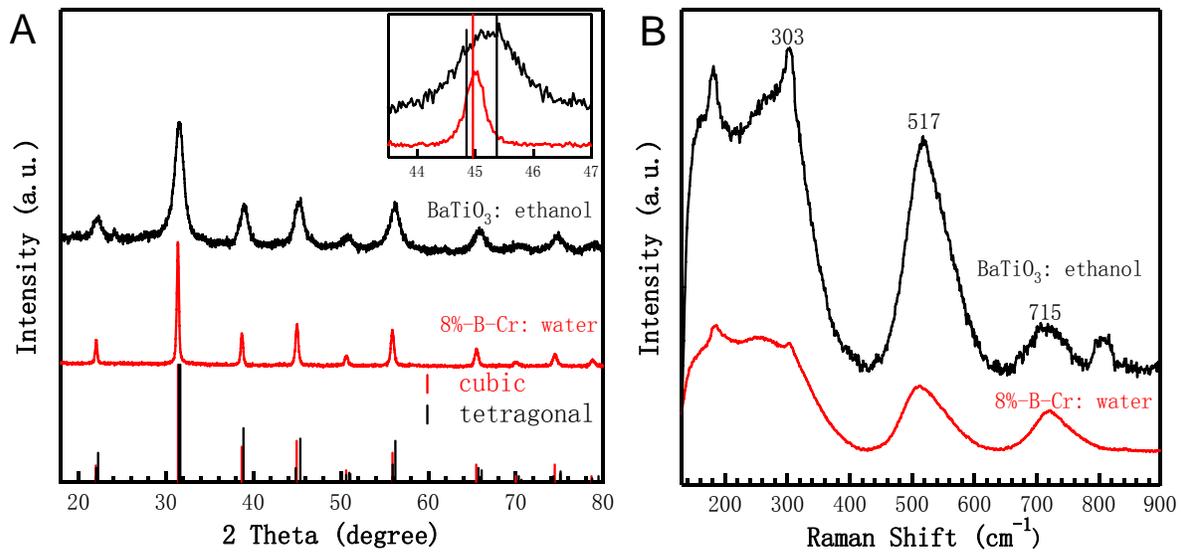
Fig. 4.10 (A) XRD patterns and (B) Raman spectra of BaTiO$_3$ nanoparticles synthesized in ethanol (black) and 8%-B Cr^{3+}-doped BaTiO$_3$ prepared in water (red).

Some parameters derived from the Raman data are shown in Table 4.2. Both the linewidths of 303 and 715 cm^{-1} peaks become broader in the Cr^{3+}-doped larger particles, implying the phase evolution induced by dopants. The difference in I$_{517}$ / I$_{715}$ values is consistent with the change in stoichiometry of nanocrystals doped by Cr^{3+} ions. Thus, in comparison to ethanol-synthesized nanocrystals in which particle size is decreased 20 times and tetragonality is therefore weakened to some extent, the dopant effect can be stronger in promoting the phase transition to cubic form by lessening the tetragonality in the highly Cr^{3+}-doped BaTiO$_3$ even the size remains the same as the undoped ones.

Table 4.2 Comparison of Raman data of BaTiO$_3$ nanoparticles synthesized in ethanol and 8%-B Cr^{3+}-doped BaTiO$_3$ prepared in water.

Sample	Linewidth at 303 cm^{-1}	Linewidth at 715 cm^{-1}	I$_{517}$/ I$_{715}$
BaTiO$_3$: ethanol	37 cm^{-1}	115 cm^{-1}	5.40
8%-B-Cr: water	81 cm^{-1}	192 cm^{-1}	0.98

In fact, the so-called size effect of BaTiO$_3$ nanoparticles has been widely studied. Possible reasons such as depolarization effects, the absence of long-range interactions, structural defects and elastic constraints were explained in Chapter 1. However the dopant induced tetragonal-to-cubic phase transition behavior at room temperature has not been systematically investigated. In this project, by substituting the Ti^{4+} by Cr^{3+} ions in BaTiO$_3$ nanocrystals with size ranging from 5 to 200 nm and characterizing the phase evolution by XRD and Raman spectrum measurements, we presented a consistent trend of the dopant effect on ferroelectric phase transition in BaTiO$_3$ nanocrystals.

It is proposed that the main reason for the dopant effect is the lack of driving force associated with Ti-O hybridization which stabilizes the Ti^{4+} off-center displacement. As most ferroelectric oxide perovskites (ABO$_3$) have B cations with d^0 states, the Ti 3d and O 2p hybridization in BaTiO$_3$ is essential to soften the electric repulsions and thus allows for the disordered tetragonal phase at room temperature. While Cr^{3+} have a 3d^3 electron structure, and is unable to provide the unoccupied energy levels d^0 states to hybridize with the O 2p ions.

When it is sitting in the center of the O_6 octahedron, the bonding between Cr^{3+} and O^{2-} should be more ionic compared with the partial covalent Ti-O interaction, so no specific driving force is provided to soften the short-range ion-ion repulsion. As a result, the ferroelectric displacement of Cr^{3+} in the cage of six O^{2-} sites does not readily occur. In this sense, the cubic phase with higher symmetry is preferred. Therefore, the occupancy of d orbital in the doped transition metal ions is likely to influence the structure and further the ferroelectric properties of $BaTiO_3$ nanocrystals.

On the other hand, the defects accompanied by dopant in the crystal lattice are not negligible. Though the OH⁻ group is found not to be en essential factor to quench the tetragonal phase through Raman data, other defects are still present in the doping system. Oxygen vacancies, for example, are common defects observed in the doped semiconductor nanocrystals. The density of oxygen vacancies is increased when more dopant is incorporated into the host material. We suppose this mobile vacancy defects might be responsible for the phase transition behavior of $BaTiO_3$ nanocrystals, though no direct proof has been obtained right now. Also, the lattice expansion associated with the substitution of Ti^{4+} with Cr^{3+} can be another reason for the phase transition. To clarify this complex effect of dopant on nanocrystal structure, further research will be required.

4.6 Magnetic Measurements

Fig. 4.11 shows the 2 K saturation magnetization of 10% Cr^{3+}-doped $BaTiO_3$ powder

synthesized in benzyl alcohol (dots) along with the close fit to the spin-only Brillouin function

described by equation 4.1, using S = 3/2 (d^3 system with total spin quantum number of S =

3/2) and the Landé g-factor of 1.974 characteristic for Cr^{3+} in $BaTiO_3$ ceramics.[88]

$$B(x) = (2S+1)[coth((2S+1)(g\mu_BH/2k_BT)) - coth((g\mu_BH/2k_BT))]$$ **(equation 4.1)**

In this equation, μ_B is the Bohr magneton, k_B is the Boltzmann constant, T is the temperature,

and H is the applied magnetic field. The fit and experimental curves agree well. A slight

deviation, however, may arise from the small antiferromagnetic contributions, as well as some

zero-field splitting of Cr^{3+} ions. The good match demonstrates the absence of significant

orbital angular momentum in Cr^{3+} ions, and indicates that all Cr^{3+} are accounted for as

isolated paramagnetic ions without any chromium clusters or oxides, and the doping is in fact

a substitution of octahedral Ti^{4+} with Cr^{3+}.
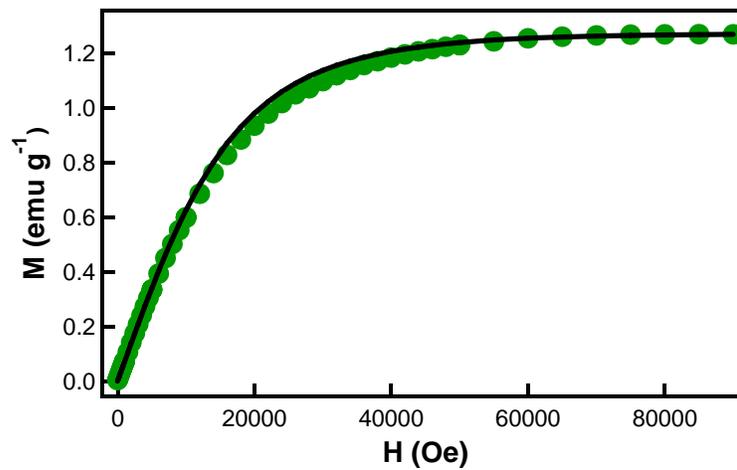
Fig. 4.11 2 K saturation magnetization of 10% Cr^{3+}-doped $BaTiO_3$ powder synthesized in

benzyl alcohol (dots). The solid line shows the S = 3/2 and g = 1.974 spin-only saturation magnetization predicted by the Brillouin function.

However, this magnetic saturation is only a preliminary measurement of the Cr^{3+}-doped $BaTiO_3$ nanocrystals. Much more characterization on the magnetization at various temperatures of both the powder and spin-coated film forms are required, in order to investigate possible ferromagnetic properties and the mechanism of magnetic ordering in doped ferroelectric oxides, which may lead to the development of multiferroics at the nanoscale.

Chapter 5   Conclusions and Future Work

5.1 Conclusions

In summary, I synthesized $BaTiO_3$ nanocrystals at different sizes by modifying the solvent composition via hydrothermal and solvothermal methods. Water, ethanol and benzyl alcohol as solvents produced nanoparticles with average sizes of 200, 10 and 5 nm, respectively. Both the XRD and TEM characterizations indicate the high purity and crystallinity of the products. Cr^{3+} ions were successfully doped into the $BaTiO_3$ host lattices with different concentrations, replacing the central Ti^{4+} ions. TOPO was found to be able to remove the surface-bound dopants and ensure internal doping. Particles of about 10 and 5 nm can dissolve well in toluene by surfactant treatment with oleic acid, leading to colloidal free-standing $BaTiO_3$ and Cr^{3+}-doped $BaTiO_3$ nanocrystals.

I observe by using XRD and Raman spectroscopy that both the size and dopants affect the room-temperature tetragonal-to-cubic phase transition in $BaTiO_3$ nanocrystals. The data suggests that the tetragonality amount is reduced from the bulk value with decreasing size, by the consistent shifting of the (200) line and disappearance of characteristic Raman peaks. However, particles as small as 10 nm retain some degree of tetragonal deformation, and a small portion of tetragonal structure in the form of Ti^{4+} displacement is even observed in particles about 5 nm. Dopant is also found to promote the phase transition as the correlation between the doping levels and the loss of tetragonality, though the average doping

concentration has not been accurately determined yet. We assume the origin of dopant effect to be a lack of driving force associated with Ti-O hybridization which stabilizes the Ti^{4+} displacement in ferroelectric tetragonal $BaTiO_3$. The interesting comparison of size and dopant effects on the phase transition behavior reveals that the latter can dominate to some extent.

Ligand-field electronic absorption spectroscopy confirms the internal substitution of Ti^{4+} with Cr^{3+}, as well as the subtle change in structures between particles at 5 and 10 nm. However, it is unable to detect any difference between various doping levels. The surface cleaning effect of TOPO is also shown in the absorption spectroscopy.

Finally, low temperature magnetic saturation suggests a good match of the experimental curve with the spin-only Brillouin function, indicating again the successful substitution of Cr^{3+} as isolated paramagnetic ions. Therefore, the Cr^{3+}-doped $BaTiO_3$ nanocrystals synthesized in this project can potentially exhibit room-temperature ferromagnetism. Combined with the ferroelectricity of pure $BaTiO_3$ lattice, this kind of material becomes a promising candidate for the multiferroics, leading to a whole range of new applications such as additional degrees of freedom in encoding and reading information electrically and magnetically.

5.2 Future Work

In order to give a clear view of dopant effect on $BaTiO_3$ phase transition, the average

doping concentrations of Cr^{3+} need to be determined. The energy dispersive X-ray (EDX) spectroscopy is not a good choice since the peak positions of Ba, Ti and Cr are too close to each other. Instead, the inductively coupled plasma atomic emission spectroscopy (ICP-AES) can be used to perform the elemental analysis.

Crystal structure refinement will provide detailed information about the lattice constants,[1, 18] which is strongly related to the phase transition. By applying a single crystal model with the XRD data, the microstructure of $BaTiO_3$ nanocrystals can be clarified, displaying how the lattice parameters and c/a ratios are changed with size and dopant influence. However, this requires high quality XRD patters such as those collected by high-energy synchrotron radiation x-rays, and a reasonable analysis method.

More magnetic measurement will be performed both in the powder and spin-coated film forms. Considering the smaller particles at 5 and 10 nm are not large enough to support a ferromagnetic domain while the 200 nm nanocrystals are able to, the magnetic data obtained for the different sized samples can lead to a deeper understanding of the origin of ferromagnetism in diluted magnetic semiconductors. It has recently been reported that in small particles, spin-coating and annealing process can create a large amount of interfacial defects, whose radii were sufficiently large to overlap many dopant ions as well as adjacent defects, causing a net alignment of the dopant spins.[67, 69]

In the long term, we would like to measure some electrical properties of both the undoped and doped $BaTiO_3$ nanocrystals, such as conductivity, dielectric and ferroelectric

properties. Furthermore, both of the ferroelectric and ferromagnetic properties have an extremely different behavior as a function of size, which may result in the observation of new phenomena and discovery of new interactions when we manipulate the size and induce dopants. We hope that examining multiferroic materials in the nanoscale region can provide a much deeper microscopic understanding of the mechanisms of these two types of ordering and their mutual relationship.

References

1.   Huang, T.-C.; Wang, M.-T.; Sheu, H.-S.; Hsieh, W.-F., Size-Dependent Lattice Dynamics of Barium Titanate Nanoparticles. *J. Phys.: Condens. Matter* **2007,** 19, 476212.

2.   Huang, L.; Chen, Z.; Wilson, J. D.; Banerjee, S.; Robinson, R. D.; Herman, I. P.; Laibowitz, R.; O'Brien, S., Barium Titanate Nanocrystals and Nanocrystal Thin Films: Synthesis, Ferroelectricity, and Dielectric Properties. *J. Appl. Phys.* **2006,** 100, 034316.

3.   Tripathy, S. S.; Raichur, A. M., Dispersibility of Barium Titanate Suspension in the Presence of Polyelectrolytes: A Review. *J. Dispersion Sci. Technol.* **2008,** 29, 230-239.

4.   Pradip; Rai, B.; Sathish, P.; Krishnamurty, S., Rational Design of Dispersants for Colloidal Processing of Barium Titanate Suspensions by Molecular Modeling. *Ferroelectr.* **2004,** 306, 195-208.

5.   Strukov, B. A.; Levanyuk, A. P., *Ferroelectric Phenomena in Crystals: Physical Foundations*. Springer-Verlag: Berlin/New York, 1998.

6.   Xu, Y., *Ferroelectric Materials and Their Applications*. North-Holland: Amsterdam, 1991.

7.   Cohen, R. E.; Krakauer, H., Lattice Dynamics and Origin of Ferroelectricity in BaTiO$_3$: Linearized-Augmented-Plane-Wave Total-Energy Calculations. *Phys. Rev. B* **1990,** 42, 6416-6423.

8.   Blinc, R., Order and Disorder in Perovskites and Relaxor Ferroelectrics. *Struct Bond* **2007,** 124, 51-67.

9.   Yu, J.; Chu, J., Nanocrystalline Barium Titanate. *Encycl. Nanosci. Nanatechnol.* **2004,** 6, 389-416.

10. Saha, S.; Sinha, T. P., Electronic Structure, Chemical Bonding, and Optical Properties of Paraelectric BaTiO$_3$. *Phys. Rev. B* **2000,** 62, 8828.

11. Cohen, R. E., Origin of Ferroelectricity in Perovskite Oxides. *Nature* **1992,** 358, 136-138.

12. Hill, N. A., Why Are There so Few Magnetic Ferroelectrics? *J. Phys. Chem. B* **2000,** 104, 6694-6709.

13. Cohen, R. E., Theory of Ferroelectrics: a Vision for the Next Decade and Beyond. *J. Phys. Chem. Solids* **2000,** 61, 139-146.

14. Fillippetti, A.; Hill, N. A., Coexistence of Magnetism and Ferroelectricity in Perovskites. *Phys. Rev. B* **2002,** 65, 159120.

15. Sun, W., Size Effect in Barium Titanate Powders Synthesized by Different Hydrothermal Methods. *J. Appl. Phys.* **2006,** 100, 083503.

16. Yun, W. S.; Urban, J. J.; Gu, Q.; Park, H., Ferroelectric Properties of Individual Barium Titanate Nanowires Investigated by Scanned Probe Microscopy. *Nano Lett.* **2002,** 2, 447-450.

17. Ahn, C. H.; Rabe, K. M.; Triscone, J. M., Ferroelectricity at the Nanoscale: Local Polarization in Oxide Thin Films and Heterostructures. *Science* **2004,** 303, 488-491.

18. Smith, M. B.; Page, K.; Siegrist, T.; Redmond, P. L.; Walter, E. C.; Seshadri, R.; Brus, L. E.; Steigerwald, M. L., Crystal Structure and the Paraelectric-to-Ferroelectric Phase Transition of Nanoscale BaTiO$_3$. *J. Am. Chem. Soc.* **2008,** 130, 6955-6963.

19. Sedykh, P.; Michel, D., Ferroelectric Phase Transition in Barium Titanate Nanoparticles. *Phys. Rev. B* **2009,** 79, 134119.

20. Frey, M. H.; Payne, D. A., Grain-Size Effect on Structure and Phase Transformations for Barium Titanate. *Phys. Rev. B* **1996,** 54, 3158-3168.

21. Uchino, K.; Sadanaga, E.; Hirose, T., Dependence of Crystal Structure on Particle Size in Barium Titantate. *J. Am. Ceram. Soc.* **1989,** 72, 1555-1558.

22. Spanier, J. E.; Kolpak, A. M.; Urban, J. J.; Grinberg, I.; Ouyang, L.; Yun, W. S.; Rappe, A. M.; Park, H., Ferroelectric Phase Transition in Individual Single-Crystalline BaTiO$_3$ Nanowires. *Nano Lett.* **2006,** 6, 735-739.

23. Petkov, V.; Gateshki, M.; Niederberger, M.; Ren, Y., Atomic-Scale Structure of Nanocrystalline Ba$_x$Sr$_{1-x}$TiO3 (x = 1, 0.5, 0) by X-ray Diffraction and the Atomic Pair Distribution Function Technique. *Chem. Mater.* **2006,** 18, 814-821.

24. Zalar, B.; Laguta, V. V.; Blinc, R., NMR Evidence for the Coexistence of Order-Disorder and Displacive Components in Barium Titanate. *Phys. Rev. Lett* **2003,** 90, 037601.

25. Hoshina, T.; Kakemoto, H.; Tsurumi, T.; Wada, S., Size and Temperature Induced Phase Transition Behaviors of Barium Titanate Nanparticles. *J. Appl. Phys.* **2006,** 99, 054311.

26. Lines, M. E.; Glass, A. M., *Principles and Applications of Ferroelectrics and Related Materials*. Clarendon: Oxford, 1977.

27. Chattopadhyay, S.; Ayyub, P.; Palkar, V. R.; Multani, M., Size-Induced Diffuse Phase

Transition in the Nanocrystalline Ferroelectric PbTiO3. *Phys. Rev. B* **1995,** 52, 13177.

28. Joshi, U. A.; Yoon, S.; Baik, S.; Lee, J. S., Surfactant-Free Hydrothermal Synthesis of Highly Tetragonal Barium Titanate Nanowires: A Structural Investigation. *J. Phys. Chem. B* **2006,** 110, 12249-12256.

29. Noma, T.; Wada, S.; Yano, M.; Suzuki, T., Analysis of Lattice Vibration in Fine Particles of Barium Titanate Single Crystal Including the Lattice Hydroxyl Group. *J. Appl. Phys* **1996,** 80, 5223-5233.

30. Yan, T.; Shen, Z.-G.; Zhang, W.-W.; Chen, J.-F., Size Dependence on the Ferroelectric Transition of Nanozied BaTiO$_3$ Particles. *Mater. Chem. Phys.* **2006,** 98, 450-455.

31. Begg, B. D.; Vance, E. R.; Nowotny, J., Effect of Particle Size on the Room-Temperature Crystal Structure of Barium Titanate. *J. Am. Ceram. Soc.* **1994,** 77, 3186-3192.

32. Zhu, X.; Zhu, J.; Zhou, S.; Liu, Z.; Ming, N.; Hess, D., BaTiO$_3$ Nanocrystals: Hydrothermal Synthesis and Structural Characterization. *J. Cryst. Growth* **2005,** 283, 553-562.

33. Niederberger, M.; Garnweitner, G.; Pinna, N.; Antoniett, M., Nonaqueous and Halide-Free Route to Crystalline BaTiO$_3$, SrTiO$_3$, and (Ba,Sr)TiO$_3$ Nanoparticles via a Mechanism Involving C-C Bond Formation. *J. Am. Chem. Soc.* **2004,** 126, 9120-9126.

34. O'Brien, S.; Brus, L.; Murray, C. B., Synthesis of Monodisperse Nanoparticles of Barium Titanate: Toward a Generalized Strategy of Oxide Nanoparticle Synthesis. *J. Am. Chem. Soc.* **2001,** 123, 12085-12086.

35. Lencka, M. M.; Riman, R. E., Thermodynamic Modelin of Hydrothermal Synthesis of Ceramic Powders. *Chem. Mater.* **1993,** 5, 61-70.

36. Yamamoto, T.; Urabe, K.; Banno, H., BaTiO$_3$ Particle-Size Dependence of Ferroelectricity in BaTiO$_3$/Polymer Composites. *Jpn. J. Appl. Phys.* **1993,** 77, 4272-4276.

37. Park, J. K.; Park, S. D., Synthesis of Barium Titanate by Hydrothermal Method and Its Formation Mechanisms. *J. Chem. Eng. Jpn.* **2008,** 41, 631-638.

38. Hu, M. Z.-C.; Kurian, V.; Payzant, E. A.; Rawn, C. J.; Hunt, R. D., Wet-Chemical Synthesis of Monodispersed Barium Titanate Particles- Hydrothermal Conversion of TiO$_2$ Microspheres to Nanocrystalline BaTiO$_3$. *Powder Technol.* **2000,** 110, 2-14.

39. Niederberger, M.; Bartl, M. H.; Stucky, G. D., Benzyl Alcohol and Transition Metal Chlorides as Versatile Reaction System for the Nonaqueous and Low-Temperature Synthesis

of Crystalline Nano-Objects with Controlled Dimensionality. *J. Am. Chem. Soc.* **2002,** 124, 13642-13643.

40. Niederberger, M.; Pinna, N.; Polleux, J.; Antonietti, M., A General Soft-Chemistry Route to Perovsites and Related Materials: Synthesis of $BaTiO_3$, $BaZrO_3$, and $LiNbO_3$ Nanoparticles. *Angew. Chem. Int. Ed.* **2004,** 43, 2270-2273.

41. Wei, X.; Xu, G.; Ren, Z.; Wang, Y.; Shen, G.; Han, G., Synthesis of Highly Dispersed Barium Titanate Nanoparticles by a Novel Solvothermal Method. *J. Am. Ceram. Soc.* **2008,** 91, 315-318.

42. Erwin, S. C.; Zu, L.; Haftel, M. I.; Efros, A. L.; Kennedy, T. A.; Norris, D. J., Doping Semiconductor Nanocrystals. *Nature* **2005,** 436, 91-94.

43. Norris, D. J.; Efros, A. L.; Erwin, S. C., Doped Nanocrystals. *Science* **2008,** 319, 1776-1779.

44. Stamplecoskie, K. G.; Ju, L.; Farvid, S. S.; Radovanovic, P. V., General Control of Transition-Metal-Doped GaN Nanowire Growth: Toward Understanding the Mechanism of Dopant Incorporation. *Nano Lett.* **2008,** 8, 2674-2681.

45. Alivisatos, A. P., Semiconductor Clusters, Nanocrystals, and Quantum Dots. *Science* **1996,** 271, 933-937.

46. Bryan, J. D.; Gamelin, D. R., Doped Semiconductor Nanocrystals: Synthesis, Characterization, Physical Properties, and Applications. *Prog. Inorg. Chem.* **2005,** 54, 47-126.

47. Prades, M.; Maso, N.; Beltran, H.; Cordoncillo, E.; West, A. R., Polymorphism of $BaTiO_3$ Acceptor Doped with Mn^{3+}, Fe^{3+}, and Ti^{3+}. *J. Am. Ceram. Soc.* **2008,** 91, 2364-2366.

48. Buscaglia, M. T.; Buscaglia, V.; Viviani, M.; Nanni, P.; Hanuskova, M., Influence of Foreign Ions on the Crystal Structure of $BaTiO_3$. *J. Euro. Ceram. Soc.* **2000,** 20, 1997-2007.

49. Brutchey, R. L.; Cheng, G.; Gu, Q.; Morse, D. E., Positive Temperature Coefficient of Resistivity in Donor-Doped $BaTiO_3$ ceramics Derived from Nanocrystals Synthesized at Low Temperature. *Adv. Mater.* **2008,** 20, 1029-1033.

50. Maso, N.; Beltran, H.; Cordoncillo, E.; Flores, A. A.; Escribano, P.; Sinclair, D. C.; West, A. R., Synthesis and Electrical Properties of Nb-doped $BaTiO_3$. *J. Mater. Chem.* **2006,** 16, 3114-3119.

51. Buscaglia, M. T.; Buscaglia, B.; Viviani, M., Atomistic Simulation of Dopant Incorporation in Barium Titanate. *J. Am. Ceram. Soc.* **2001,** 84, 376-384.

52. Kundu, T. K.; Jana, A.; Barik, P., Doped Barium Titanate Nanoparticles. *Bull. Mater. Sci.* **2008,** 31, 501-505.

53. Kirianov, A.; Ozaki, N.; Ohsato, H.; Kohzu, N.; Kishi, H., Studies on the Solid Solution of Mn in $BaTiO_3$. *Jpn. J. Appl. Phys.* **2001,** 40, 5620-5623.

54. Langhammer, H. T.; Muller, T.; Felgner, K.-H.; Abicht, H.-P., Crystal Structure and Related Properties of Manganese-Doped Barium Titanate Ceramics. *J. Am. Ceram. Soc.* **2000,** 83, 605-611.

55. Nakayama, H.; Katayama-Yoshida, H., Theoretical Prediction of Magnetic Properties of $Ba(Ti_{1-x}Mn_x)O_3$ (M=Sc, V, Cr, Mn, Fe, Co, Ni, Cu). *Jpn. J. Appl. Phys.* **2001,** 40, 1355-1358.

56. Ray, S.; Mahadevan, P.; Mandal, S.; Krishnakumar, S. R.; Kuroda, C. S.; Sasaki, T., High Temperature Ferromagnetism in Single Crystalline Dilute Fe-Doped $BaTiO_3$. *Phys. Rev. B* **2008,** 77, 104416.

57. Tong, X.; Lin, Y.-H.; Zhang, S.; Wang, Y.; Nan, C.-W., Preparation of Mn-Doped $BaTiO_3$ Nanoparticles and Their Magnetic Properties. *J. Appl. Phys.* **2008,** 104, 066108.

58. Mcelfresh, M., *Fundamentals of Magnetism and Magneic Measurements*. Purdue University: 1994.

59. Wang, Z. L.; John Wiley & Sons., Characterization of Nanophase Materials. In Wiley-VCH: Weinheim, 2000.

60. Eerenstein, W.; Mathur, N. D.; Scott, J. F., Multiferroic and Magnetoelectric Materials. *Nature* **2006,** 442, 759-765.

61. Fiebig, M., Revival of the Magnetoelectric Effect. *J. Phys. D* **2005,** 38, 123-152.

62. Dalpian, G. M.; Chelikowsky, J. R., Self-Purification in Semiconductor Nanocrystals. *Phys. Rev. Lett.* **2006,** 96, 226802.

63. LaMer, V. K.; Dinegar, R. H., Theory, Production and Mechanism of Formation of Monodispersed Hydrosols. *J. Am. Chem. Soc.* **1950,** 72, 4847-4854.

64. Oxtoby, D. W., Nucleation of First-Order Phase Transitions. *Acc. Chem. Res.* **1998,** 31, 91-97.

65. Davis, K. J.; Dove, P. M.; Yoreo, J. J. D., The Role of Mg^{2+} as an Impurity in Calcite Growth. *Science* **2000,** 290, 1134-1137.

66. Schwartz, D. A.; Norberg, N. S.; Nguyen, Q. P.; Parker, J. M.; Gamelin, D. R., Magnetic Quantum Dots: Synthesis, Spectroscopy, and Magnetism of Co^{2+}- and Ni^{2+}-Doped ZnO Nanocrystals. *J. Am. Chem. Soc.* **2003,** 125, 13205-13218.

67. Bryan, J. D.; Santangelo, S. A.; Keveren, S. C.; Gamelin, D. R., Activation of High-T_C Ferromagnetism in Co^{2+}:TiO$_2$ and Cr^{3+}:TiO$_2$ Nanorods and Nanocrystals by Grain Boundary Defects. *J. Am. Chem. Soc.* **2005,** 127, 15568-15574.

68. Farvid, S. S.; Ju, L.; Worden, M.; Radovanovic, P. V., Colloidal Chromium-Doped In_2O_3 Nanocrystals as Building Blocks for High-T_C Ferromagnetic Transparent Conducting Oxide Structures. *J. Phys. Chem. C* **2008,** 112, 17755-17759.

69. Archer, P. I.; Radovanovic, P. V.; Heald, S. M.; R.Gamelin, D., Low -Temperature Activation and Deactivation of High-Curie-Temperature Ferromagnetism in a New Diluted Magnetic Semiconductor: Ni^{2+}-Doped SnO_2. *J. Am. Chem. Soc.* **2005,** 127, 14479-14487.

70. Smart, L.; Moore, E., *Solid State Chemistry : An Introduction*. CRC Press: Boca Raton, 2005.

71. Ferraro, J. R.; Nakamoto, K., *Introductory Raman Spectroscopy*. Academic Press Inc.: San Diego, 2003.

72. Kolen'ko, Y. V.; Kovnir, K. A.; Neira, I. S.; Taniguchi, T.; Ishigaki, T.; Watanabe, T.; Sakamoto, N.; Yoshimura, M., A Novel, Controlled, and High-Yield Solvothermal Drying Route to Nanosized Barium Titanate Powders. *J. Phys. Chem. C* **2007,** 111, 7306-7318.

73. Shiratori, Y.; Pithan, C.; Dornseiffer, J.; Waser, R., Raman Scattering Studies on Nanocrystalline BaTiO$_3$ Part I - Isolated Particles and Aggregates. *J. Raman Spectrosc.* **2007,** 38, 1288-1299.

74. Kwon, S.-G.; Park, B.-H.; Choi, K.; Choi, E.-S.; Nam, S.; Kim, J.-W.; Kim, J.-H., Solvothermally Synthesized Tetragonal Barium Titanate Powders Using H$_2$O/EtOH Sovent. *J. Euro. Ceram. Soc.* **2006,** 26, 1401-1404.

75. Wei, X.; Xu, G.; Ren, Z.; Wang, Y.; Shen, G.; Han, G., Size-Controlled Synthesis of BaTiO$_3$ Nanocrystals via a Hydrothermal Route. *Mater. Lett.* **2008,** 62, 3666-3669.

76. Niederberger, M., Nonaqueous Sol-Gel Routes to Metal Oxide Nanoparticles. *Acc. Chem. Res.* **2007,** 40, 793-900.

77. Suyama, Y.; Noritake, T.; Nagasawa, M., Formation of BaTiO$_3$ from a Barium Titanium Isopropoxide Complex. *Jpn. J. Appl. Phys.* **1997,** 36, 5939-3942.

78. Wang, Q.; Xu, G.; Han, G., Solvothermal Synthesis and Characterization of Uniform CdS Nanowires in High Yield. *J. Solid State Chem.* **2005,** 178, 2680-2685.

79. Venkateswaran, U. D.; Naik, V. M.; Naik, R., High-Pressure Raman Studies of Polycrystalline BaTiO3. *Phys. Rev. B* **1998,** 58, 14256-14260.

80. Chen, M. S.; Shen, Z. X.; Tang, S. H.; Shi, W. S.; Cui, D. F.; Chen, Z. H., Stress effect on Raman Spectra of Ce-doped BaTiO$_3$ Films. *J. Phys.: Condens. Matter* **2000,** 12, 7013-7023.

81. Wada, S.; Suzuki, T.; Osada, M.; Katihana, M.; Noma, T., Change of Macroscopic and Microscopic Symmetry of Barium Titanate Single Crystal around Curie Temperature. *Jpn. J. Appl. Phys.* **1998,** 37, 5385-5393.

82. Denton, A. R.; Ashcroft, N. W., Vegard's Law. *Phys. Rev. A* **1991,** 43, 3161-3164.

83. Robins, L. H.; Kaise, D. L.; Rotter, L. D.; Schenck, P. K.; Stauf, G. T.; Rytz, D., Investigation of the Structure of Barium Titanate Thin Film by Raman Spcetroscopy. *J. Appl. Phys.* **1994,** 76, 7487-7498.

84. Urban, M. W.; Cornilsen, B. C., Measurement of Nonstoichiometry in BaTiO$_3$ Using Raman Spectroscopy. In *Advances in Material Characterization II*, Snyder, R. L.; Condrate, R. A.; Johnson, P. F., Eds. Plenum Press: New York, 1985; pp 89-96.

85. Busca, G.; Buscaglia, V.; Leoni, M.; Nanni, P., Solid-State and Surface Spectroscopic Characterization of BaTiO$_3$ Fine Powders. *Chem. Mater.* **1994,** 6, 955-961.

86. Katari, J. E. B.; Colvin, V. L.; Alivisatos, A. P., X-ray Photoelectron Spectroscopy of CdSe Nanocrystals with Applications to Studies of the Nanocrystal Surface. *J. Phys. Chem.* **1994,** 98, 4109-4117.

87. Tsunekawa, S.; Ito, S.; Mori, T.; Ishikawa, K.; Li, Z.-Q.; Kawazoe, Y., Critical Size and Anomalous Latice Expansion in Nanocrystalline BaTiO$_3$ Particles. *Phys. Rev. B* **2000,** 62, 3065-3070.

88. Langhammer, H. T.; Muller, T.; Bottcher, R.; Abicht, H.-P., Structural and Optical Properties of Chromium-Doped Hexagonal Barium Titanate Ceramics. *J. Phys.: Condens. Matter* **2008,** 20, 085206.